communications earth & environment | Article
A Nature Portfolio journal

https://doi.org/10.1038/s43247-025-02359-1

Drought risks are projected to increase in the future in central and southern regions of the Middle East

Check for updates

Younes Khosravi & Taha B. M. J. Ouarda

Drought prediction is vital for sustaining water security in regions highly exposed to climate change. Here we present a machine learning-based method that integrates climate model outputs to improve drought monitoring in the Middle East. We introduce a spatially adaptive index called the Geographically Weighted Temperature Vegetation Dryness Index, developed using local regression techniques and trend analysis. This index integrates temperature and vegetation signals while accounting for variations across space and time. It substantially improves prediction accuracy compared to previous methods. We used recent climate projections under three socioeconomic scenarios to estimate future drought patterns. Results show spatial shifts and intensification of drought conditions in parts of the region by the end of the century under high-emission conditions. Our method also detects localized drought hotspots that broader indices may miss, offering valuable insights for targeted and adaptive water resource planning.

In recent decades, both natural variability and human-induced climate change have driven remarkable shifts in global weather patterns, profoundly impacting water resources, agriculture, and ecosystems[1–3]. However, growing evidence highlights that anthropogenic factors such as greenhouse gas emissions and land-use changes are key contributors to the increasing frequency and intensity of meteorological disasters worldwide[4]. The situation is especially pronounced in arid and semi-arid regions, including the Middle East, where water scarcity and drought pose serious threats to the sustainability of natural resources and long-term food security[5–9]. Rising temperatures not only profoundly impacts hydrological processes[10] but also drives profound changes in regional climates, leading to more frequent and intense extreme events such as droughts and heat stress[11]. According to the Fifth Assessment Report (AR5) of the Intergovernmental Panel on Climate Change, a global mean temperature increase of 0.85 °C between 1880 and 2012 has already heightened the frequency of meteorological disasters including droughts, floods, and typhoons[12].

Drought is among the most devastating outcomes of climate change, ranking second only to floods in its global impact and affecting ~7.5% of the population[13,14]. Its far-reaching repercussions include diminished natural resources, reduced agricultural productivity, constrained water availability, disrupted ecological functions, and compromised economic resilience in local communities[15–18]. As climate change accelerates, rising global temperatures and shifting precipitation patterns are not only increasing the frequency of drought events but also amplifying their intensity, with arid and semi-arid regions facing the most severe impacts[19–21]. Reliable drought prediction and efficient water resource management can help mitigate such adverse consequences and reduce economic losses[22–24]. Thus, developing sophisticated predictive systems and employing innovative scientific approaches to lessen drought impacts and ensure sustainable resource management is an urgent global priority[25,26].

The growing complexity and unpredictability of droughts under climate change challenge traditional monitoring and prediction methods. Classical drought indices, such as the Palmer Drought Severity Index (PDSI)[27], the Standardized Precipitation Index (SPI)[28], the Standardized Precipitation Evapotranspiration Index[29], and the self-calibrating PDSI[30], provide global-scale drought assessments but often lack the spatial and temporal resolution needed for accurate local drought monitoring. These indices, originally developed for large-scale applications, are often insufficient for capturing fine-scale drought variations in regions with complex topography and heterogeneous climate conditions[31,32]. Studies have shown that traditional drought indices may fail to reflect regional drought conditions accurately, especially in areas where land surface-atmosphere interactions play a significant role in drought development[33,34]. Recognizing these limitations, the development of integrated and localized drought indices has emerged as a critical necessity[35]. Localized drought indices, such as the Geographically Weighted Temperature Vegetation Dryness Index (GWTVDI), incorporate high-resolution climatic and topographical data to improve drought monitoring accuracy. Unlike traditional drought indices,

Canada Research Chair in Statistical Hydro-Climatology, Institut National de la Recherche Scientifique, Centre Eau Terre Environnement, INRS-ÉTÉ, Québec, QC, Canada. e-mail: Younes.khosravi@inrs.ca; taha.ouarda@inrs.ca

which assume spatial stationarity, localized indices leverage advanced statistical techniques such as Geographically Weighted Regression (GWR) to account for spatial heterogeneity, improving prediction performance at finer scales[33]. Recent studies have emphasized that localized drought indices, when integrated with high-resolution climate projections, provide a more accurate assessment of drought severity, particularly in water-scarce regions like the Middle East[36–38]. Accordingly, the Middle East was selected as the evaluation domain in this study, given its acute vulnerability to drought, substantial climatic diversity, and projected increase in future drought severity[39–41]. These characteristics make it an ideal and high-priority region for testing the effectiveness of advanced drought indices in capturing local variations and enhancing climate resilience. However, these conventional approaches often struggle to capture intricate spatiotemporal dynamics and the complex interplay among climatic, hydrological, and ecological factors interactions that are increasingly significant in a changing climate[42,43]. Recognizing these limitations, the development of integrated and localized indices has emerged as a critical necessity[44,45]. To address these challenges, this study introduces the GWTVDI. This index harnesses advanced GWR while incorporating key climatic variables such as precipitation, temperature, and evaporation as well as geographical parameters (e.g., latitude, longitude, elevation, slope, and aspect). By further integrating a Mann–Kendall-based trend analysis, GWTVDI accounts for both spatial heterogeneity and temporal dynamics, thereby refining drought monitoring beyond the static limitations of older indices. This localized, trend-sensitive framework captures subtle variations in drought onset, severity, and duration, offering critical insights for proactive resource management and long-term planning.

While localized indices like GWTVDI address these challenges, General Circulation Models (GCMs) remain essential for broader climatic assessments. However, GCMs, despite their significance for long-term climate predictions, are insufficient as standalone tools for accurate local-scale drought forecasting due to their low spatial resolution (100–300 km) and challenges in capturing small-scale climatic variations[46,47]. These limitations further underscore the importance of integrating localized indices with GCM outputs to enhance prediction accuracy. By combining the spatial specificity of localized indices with the broader climatic trends offered by GCMs, this integration provides a promising pathway to enhance prediction accuracy[48,49]. Such synergy bridges the resolution gap, providing actionable insights for drought mitigation and supporting precise monitoring, improved forecasting, and adaptive strategies tailored to local needs, particularly in regions vulnerable to water scarcity and extreme weather events.

Recent advances in machine learning (ML) have substantially improved drought prediction by enabling the processing of complex datasets and uncovering nonlinear relationships often missed by traditional methods[50]. These techniques have enhanced climate model ensembles and contributed to reducing uncertainties in climate projections[51,52]. However, challenges such as data quality issues including observational biases and missing records[53,54], limited interpretability in deep learning models[40,41,55], and computational burdens in handling high-dimensional climate data[39] continue to constrain their effectiveness. To address these limitations, ensemble learning approaches have gained attention, especially when combined with high-resolution datasets like CMIP6, to improve prediction accuracy and reduce uncertainty[56–59]. Widely used ML algorithms such as Random Forest (RF), Gradient Boosting (GB), XGBoost, LightGBM, and Support Vector Machine (SVM) have demonstrated strong capabilities in forecasting drought and mapping spatial patterns across diverse regions. Several studies confirm these advances: for example, ML-enhanced ensembles have improved projections of precipitation and temperature[60], assessed future drought impacts on crop yields[61], and outperformed traditional methods in predictive accuracy[62–64]. Despite these successes, single ML models often fail to fully capture the complex interdependencies among climate variables. To overcome this, ensemble strategies particularly stacking have emerged. Stacking integrates multiple base models through a meta-learner, improving generalization and reducing sensitivity to data sparsity[65–67]. This method has been applied effectively to predict variables such as temperature[25,68,69], precipitation[65,70,71], and soil moisture[72–74]. However, its application specifically in drought prediction remains limited. Nonetheless, some efforts have begun to explore this potential. For instance, stacking has been used for drought vulnerability mapping in Iran[75], soil moisture estimation in the Tibetan Plateau[76], and agricultural drought forecasting in Kenya and India[77]. In South Asia, ensemble ML models have supported regional drought projections and assessments of agricultural impacts[61]. Other studies have enhanced CMIP6-based rainfall and drought estimates using hybrid ML approaches and satellite data[78–80]. In summary, while ML and ensemble learning methods have advanced drought prediction capabilities, the targeted use of stacking models with CMIP6 data for this purpose is still limited representing a key research gap that this study seeks to fill.

This study presents a methodological framework that markedly advances the state-of-the-art in drought prediction by integrating spatial and temporal dimensions into a unified model. The core innovation lies in the development of the GWTVDI, which synergistically combines Geographically Weighted Regression (GWR) with the modified Mann–Kendall trend analysis to capture both local spatial heterogeneities and non-stationary temporal dynamics in climate variables. This spatiotemporal design enables the detection of fine-scale drought signals and evolving climatic patterns that traditional indices such as Temperature Vegetation Dryness Index (TVDI) often overlook. Moreover, the framework incorporates a stacking-based ensemble machine learning approach to refine climate projections derived from CMIP6 models, thereby enhancing predictive resolution and reducing uncertainty. By integrating topographic factors, trend indicators, and advanced machine learning outputs, GWTVDI not only improves accuracy but also facilitates the early identification of high-risk drought hotspots. These methodological advances collectively offer a robust tool for climate-resilient water management in arid and data-scarce regions such as the Middle East.

Building on the strengths of these ensemble methods, this study introduces a stacking ensemble model designed for high-precision drought prediction. Our approach proceeds in four phases: (1) calculating TVDI for the historical period across the Middle East; (2) identifying high-performing ML algorithms (HPMLA) and high-accuracy scenarios (HAC) for historical TVDI modeling using RF, XGBoost, LightGBM, CatBoost, and SVM; (3) implementing a stacking-ensemble ML model to predict maximum temperature, minimum temperature, and precipitation under three CMIP6 scenarios (SSP1-2.6, SSP2-4.5, SSP5-8.5), followed by TVDI predictions under these same scenarios; and (4) employing GWR to introduce GWTVDI, an integrated model of drought monitoring that accounts for both temporal trends and spatial heterogeneity. By integrating multivariate climatic and topographic datasets with machine learning, this study proposes, to the best of our knowledge, a new approach to address the challenges of localized drought prediction, offering actionable insights for adaptive water management and climate change mitigation strategies. Another contribution of this study is the development of a hybrid model that integrates the Modified Mann-Kendall Test and GWR to simultaneously account for temporal trends and spatial patterns in drought analysis. The results confirm that this combined framework markedly enhances predictive performance and captures evolving drought dynamics with greater spatial precision than conventional approaches.

Results

Performances of the individual ML models for TVDI historical

The predictive performance of five machine learning models (i.e., XGBoost, CatBoost, RF, SVM, and LSTM) were evaluated for forecasting the TVDI under two scenarios with different input variables (Table 1). The results in Table 1 are based on performance metrics derived from the final test subset (20% of the data), which remained completely unseen during training. The evaluation followed an 80–20 train–test split along with a 5-fold cross-validation procedure for hyperparameter tuning. This approach ensures that the reported performance accurately reflects the generalization capability of the models while minimizing the risk of overfitting. Scenario 1

Table 1 | comparative performance of machine learning models for TVDI prediction under two scenarios

	Model	R^2	RMSE	MAE
SC 1	XGBoost	0.8606	0.0539	0.0399
	CatBoost	0.8603	0.05402	0.04
	RF	0.8587	0.0543	0.0402
	SVM	0.8438	0.0571	0.0432
	LSTM	0.768	0.07	0.0547
SC 2	XGBoost	0.9365	0.0364	0.0269
	CatBoost	0.9372	0.0362	0.0267
	RF	0.86032	0.05402	0.04
	SVM	0.91772	0.0414	0.0299
	LSTM	0.8438	0.0571	0.0432

Table 2 | Assessment of the machine learning model's performance

Model	Tmax		Tmin		Precipitation	
	RMSE	R^2	RMSE	R^2	RMSE	R^2
RF	2.4464	0.9444	2.4621	0.9266	0.8493	0.6457
SMV	2.4580	0.9438	2.4679	0.9262	0.8535	0.6401
LGBM	2.4287	0.9452	2.4588	0.9268	0.8479	0.6476
XGB	2.4583	0.9438	2.4707	0.9261	0.8502	0.6445
CB	2.4715	0.9432	2.4819	0.9254	0.8543	0.6392

Table 3 | Performance Metrics of Meta-Model Regressors under Two Scenarios

	Model	Tmax		Tmin		Precipitation	
		RMSE	R^2	RMSE	R^2	RMSE	R^2
SC1	ANN	2.3686	0.972	2.7005	0.966	0.823	0.705
	MLR	2.3642	0.970	2.7027	0.964	0.844	0.704
	LASSO	2.3641	0.971	2.7016	0.965	0.826	0.704
SC2	ANN	1.8304	0.990	1.5006	0.988	0.689	0.821
	MLR	1.8381	0.988	1.5061	0.987	0.691	0.817
	LASSO	1.8326	0.989	1.5039	0.971	0.689	0.819

(SC1) incorporated climatic variables: precipitation, maximum temperature, and minimum temperature. Scenario 2 (SC2) expanded the input set by including Geographical parameters including longitude, latitude, elevation, slope, and aspect alongside the climatic variables. Under SC1, XGBoost and CatBoost demonstrated superior performance, achieving R^2 values of 0.8606 and 0.8603, respectively, with lower RMSE and MAE compared to the other models. The inclusion of geographical variables in SC2 markedly improved the models' predictive capabilities. CatBoost and XGBoost again outperformed the others, with R^2 values rising to 0.9372 and 0.9365, respectively, and further reductions in RMSE and MAE. These enhancements highlight the significance of integrating geographical parameters to capture spatial variability in drought conditions. The superior performance of gradient boosting algorithms, particularly CatBoost and XGBoost, can be attributed to their ability to handle complex nonlinear relationships and interactions among input variables[81]. CatBoost's handling of categorical features and mitigation of overfitting through effective regularization likely contributed to its marginally better performance[82]. The Random Forest model showed modest improvements, while SVM and LSTM exhibited relatively lower predictive accuracies in both scenarios. Based on these evaluations, CatBoost and XGBoost emerged as the top-performing models for TVDI prediction, effectively capturing the complex interactions between climatic and geographical parameters.

Performances of the stacking ensemble models

Predicting the TVDI required accurate forecasts of three essential climatic variables: maximum temperature, minimum temperature, and precipitation. To achieve this, we developed a Stacking-EML model tailored for different climate scenarios. Our modeling approach comprised two levels. In the first level, five machine learning algorithms (RF, XGBoost, LightGBM, SVM, and CatBoost) served as base models, generating initial predictions of the climatic variables (Table 2). The second level integrated the best-performing base models into meta-models specifically ANN[83,84], Multiple Linear Regression (MLR)[85], and LASSO regression[86,87] to further refine prediction accuracy (Table 3). The performance metrics in Table 2 and 3 were obtained from the final test dataset (20% of the total data), ensuring unbiased evaluation. The models were trained using an 80–20 train–test split, and hyperparameters were optimized via a 5-fold cross-validation procedure to ensure generalization and prevent overfitting.

Table 2 shows that LightGBM and RF consistently outperformed the other base models, demonstrating lower RMSE and higher R^2 across maximum temperature, minimum temperature, and precipitation forecasts. These results underscore the efficiency of gradient-boosting frameworks and ensemble-based methods (LightGBM, RF) in processing complex climatic datasets. Next, we combined these two base models with three meta-model regressors (ANN, MLR, LASSO), creating a final stacking layer under two input scenarios. Scenario 1 (SC1) utilized only climatic variables including maximum temperature, minimum temperature, and precipitation, while Scenario 2 (SC2) supplemented these with key geographical parameters (longitude, latitude, elevation, slope, aspect). As summarized in Table 3, incorporating geographic information (SC2) markedly enhanced predictive performance in the meta-model stage. For instance, the ANN's RMSE for maximum temperature decreased from 2.37 to 1.83, with R^2 improving from 0.972 to 0.990. Precipitation forecasts showed a similar gain, as RMSE dropped to 0.689 and R^2 rose to 0.821 under SC2. Overall, the ANN consistently outperformed MLR and LASSO, suggesting that nonlinear architectures can more effectively capture complex interactions among climatic and topographical variables.

Figure 1a–c offers a high-level visual comparison of model performances, effectively summarizing the relationship between RMSE and R^2 for each approach. The stacking ensemble model with ANN under SC2 achieved the highest performance among all tested frameworks, consistently surpassing individual CMIP6 models (AWI-CM-1-1-MR, MIROC6, MRI-ESM2-0), which showed higher and lower correlation coefficients. These performance metrics were further supported by 95% confidence intervals derived from fivefold cross-validation, ensuring statistical robustness. These findings underscore the limitations of raw CMIP6 outputs and highlight the advantage of a stacking approach, particularly when geographic factors are incorporated. In the final step, the HPMLA and the most accurate scenario (HAC) identified here were employed to project GWTVDI under three Shared Socioeconomic Pathways (SSP1-2.6, SSP2-4.5, and SSP5-8.5). This pipeline ensures that the best local-scale predictive strategies feed into drought assessments, improving the reliability of future projections.

Introducing GWTVDI as an index for prediction drought

Two approaches were employed to model the TVDI using GWR. In the first (basic) approach, a GWR model used the best-performing Stacking-EML outputs for maximum temperature, minimum temperature, and precipitation as auxiliary variables to estimate TVDI, thus focusing on the spatial heterogeneity of drought through local relationships among these climatic factors. In the second approach, referred to as GWTVDI, this GWR-based framework was enhanced by (a) adding key geographical features (latitude, longitude, elevation, slope, aspect) as independent variables, and (b) incorporating the Mann–Kendall-derived temporal trend indicator (as described in Eq. 8). The integration of these geographical parameters to refine GWR estimates had been previously validated in the

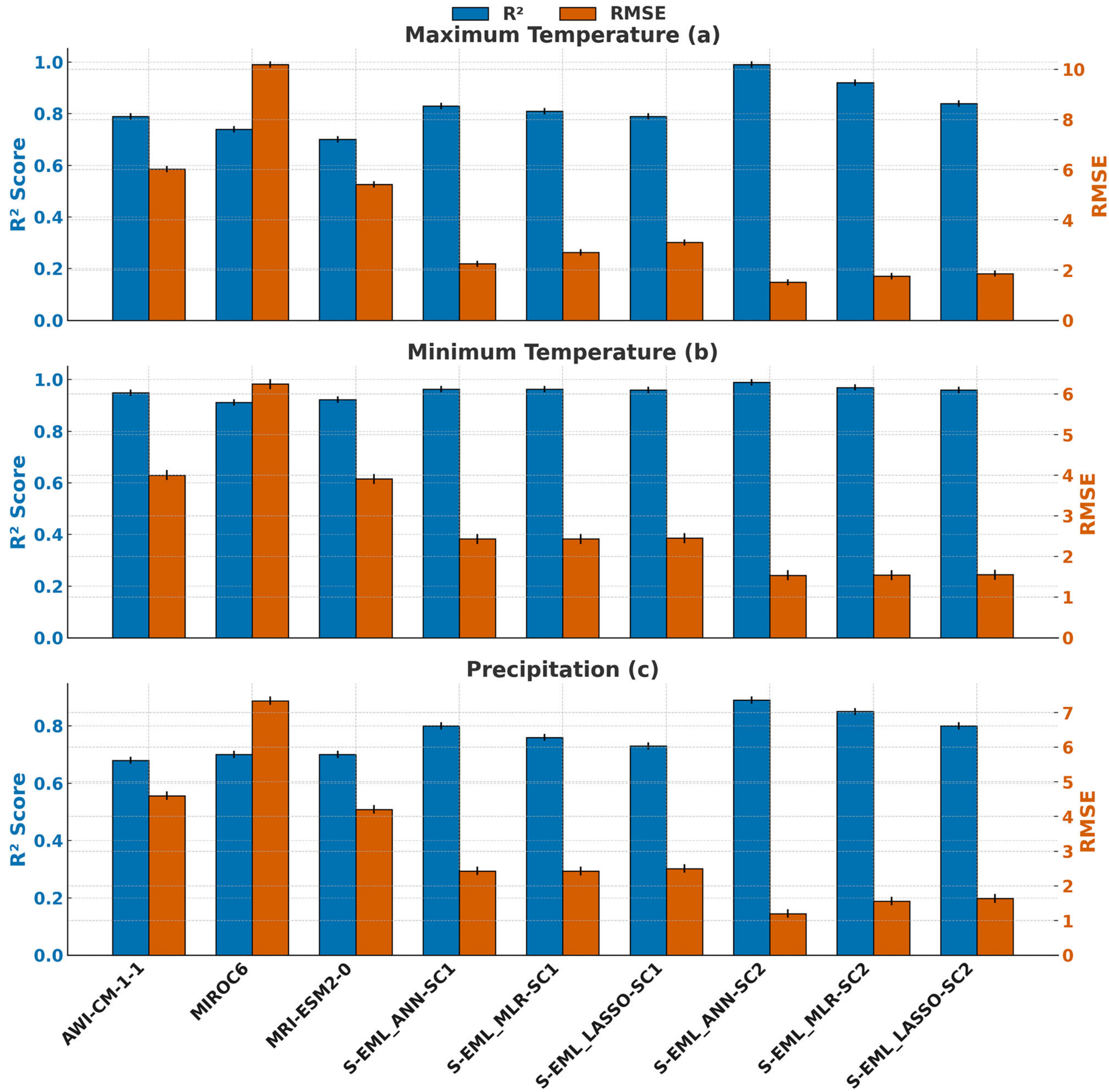

Fig. 1 | Model performance comparison for climate variable prediction. a R^2 and RMSE scores for maximum temperature predictions across individual climate models and ensemble approaches. **b** Same performance metrics for minimum temperature prediction. **c** Model performance in precipitation prediction. In all panels, blue bars represent R^2 and orange bars indicate RMSE. Models include three individual CMIP6 models (AWI-CM-1-1, MIROC6, MRI-ESM2-0) and six stacking ensemble models (S-EML) using ANN, MLR, and LASSO under two scenario configurations (SC1 and SC2). Error bars denote 95% confidence intervals from fivefold cross-validation.

study conducted by Khosravi, Homayouni and St-Hilaire[88]. By fusing local spatial weights (via GWR), temporal evolution (via Mann–Kendall trends), and a broader set of input features, GWTVDI provides a more comprehensive depiction of drought conditions across the region. Incorporating temporal trends allows the model to account for non-stationarity in the underlying climate drivers, which is especially pertinent for regions experiencing rapid changes in temperature and precipitation regimes. Thus, GWTVDI combines the strengths of geographically weighted regression, in capturing local spatial variability, with the ability to track evolving climate patterns over time. To assess which model provides greater explanatory power and predictive accuracy for drought conditions in the Middle East, two key metrics, R^2 and adjusted R^2, were utilized. Additionally, the Akaike Information Criterion corrected (AICc) was employed to evaluate model fit[89]. In this analysis, the model achieving the highest R^2 and the lowest AICc value was identified as the most appropriate based on the goodness-of-fit criteria. These metrics were computed for three SSP scenarios namely SSP1-2.6, SSP2-4.5, and SSP5-8.5 across future horizons of 2040, 2070, and 2099, thereby offering a thorough assessment of predictive performance under varying emission pathways. The resulting values are summarized in Table 4. Overall, the GWTVDI model consistently outperformed the baseline TVDI approach, as evidenced by higher Adjusted R^2 scores and more favorable AICc values across most time periods and scenarios. This observation is further supported by the Local R^2 maps (Fig. 2a–c). The data presented in these figures clearly indicate that GWTVDI outperforms TVDI in terms of R^2 values. Notably, Fig. 2 illustrates that most areas of the study region exhibit high R^2 values, underscoring the robust performance of the proposed approach in capturing the spatial variability of drought. However, certain subregions warrant closer scrutiny. Based on these maps, the central part of the study area which includes the majority of Iraq as well as eastern Iran, southeastern parts of Saudi Arabia, and portions of Egypt, exhibit significantly lower values of local R^2 (below 0.5). These lower values may indicate either greater climate variability or the influence of additional factors (e.g., groundwater abstraction, land-use change, or irrigation practices) not fully captured by the current GWTVDI formulation. Our analysis reveals that the overall number of high R^2 pixels has actually increased compared to earlier scenarios. However, a key difference lies in the spatial arrangement of these values, as the central region of the study area exhibits a more scattered and less structured pattern compared to previous scenarios. This suggests that while model accuracy remains high under SSP8.5, increasing climate variability disrupts the spatial coherence of drought predictability, likely due to intensifying hydroclimatic fluctuations. Comparing the three SSP scenarios reveals that the GWTVDI model yields the best estimates under SSP5-8.5, as evidenced by consistently superior metrics. This trend is especially notable toward the end of the century (2099), when higher emission pathways give rise to more pronounced climatic extremes, thereby accentuating the importance of modeling both local spatial heterogeneity and time-dependent signals. The superior performance of GWTVDI in these more extreme scenarios suggests that incorporating temporal trends becomes increasingly critical as climate forcings intensify, highlighting the potential of GWTVDI as a versatile tool for drought prediction in regions highly vulnerable to future climate change.

Table 4 | Comparison of AICc Values and Adjusted R^2 for TVDI and GWTVDI Models

SSP Scenario-Year	TVDI		GWTVDI	
	Adjusted R^2	AICc	Adjusted R^2	AICc
SSP2.6-2040	0.9912	−15,582.2	0.9924	−15,505.9
SSP2.6-2070	0.9811	−15,547.7	0.9816	−15,563.1
SSP2.6-2099	0.9932	−15,873.9	0.9933	−16,040.9
SSP4.5-2040	0.9832	−15,569.1	0.9836	−15,944.4
SSP4.5-2070	0.9702	−18,912.5	0.9745	−18,992.4
SSP4.5-2099	0.9845	−17,634.3	0.9897	−17,823.1
SSP8.5-2040	0.9798	−18,653.9	0.9812	−19,436.5
SSP8.5-2070	0.9909	−15,324.7	0.9955	−15,830.2
SSP8.5-2099	0.9842	−15,074.3	0.9891	−15,256.7

Spatiotemporal patterns of GWTVDI

The GWTDVI-based results reveal a gradual yet profound transformation in the spatial and temporal patterns of drought across the Middle East under three distinct climate scenarios (SSP2.6, SSP4.5, and SSP8.5) throughout the twenty-first century. Early in the period, much of the region, particularly its northern and more elevated areas, remains near normal conditions, while

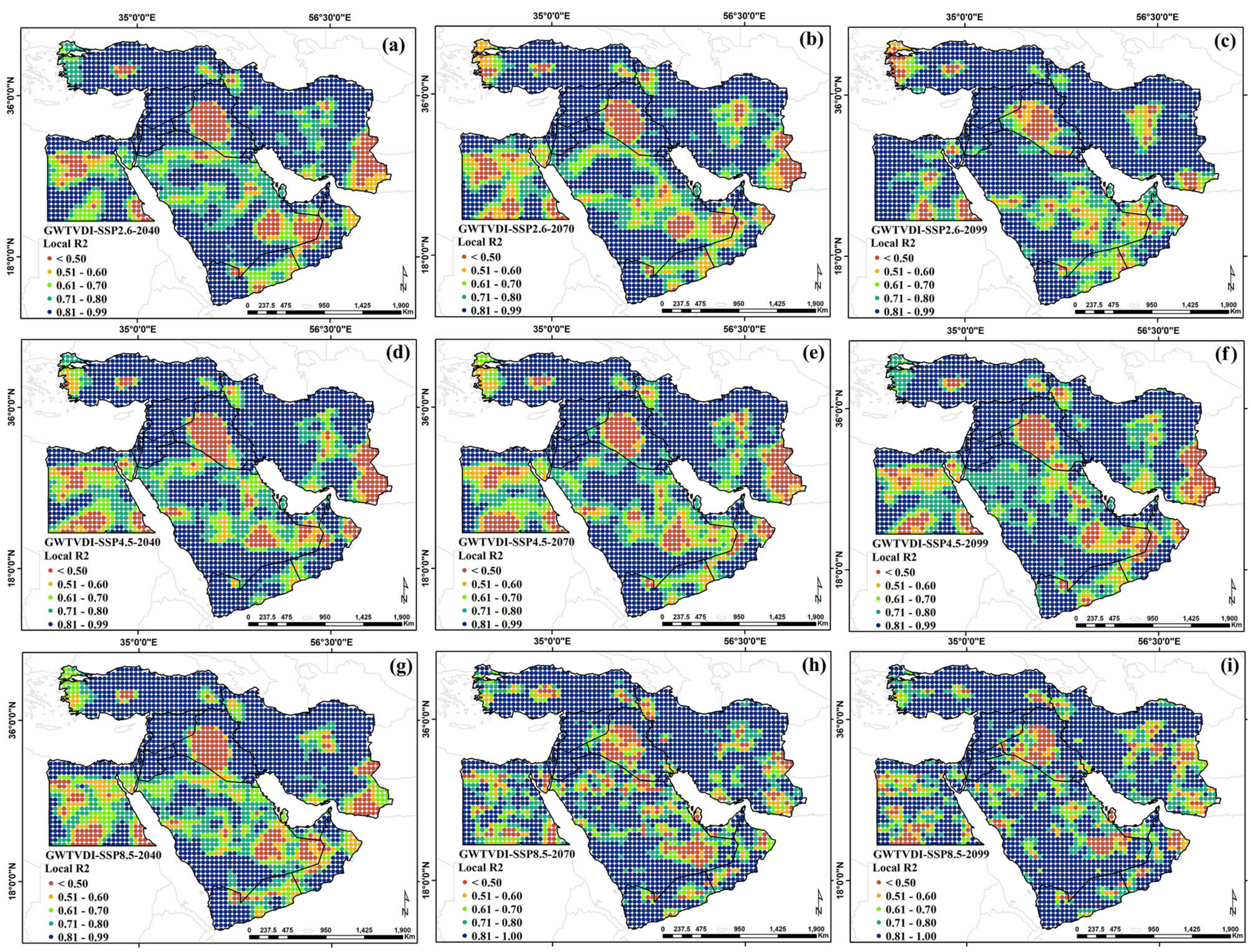

Fig. 2 | Local R^2 distribution of GWTVDI predictions under three climate scenarios for the Middle East. **a** shows local R^2 values for the year 2040 under SSP1-2.6, **b** for 2070, and **c** for 2099 under the same scenario. Under SSP2-4.5, **d** presents results for 2040, **e** for 2070, and **f** for 2099. Similarly, **g** displays local R^2 for 2040 under SSP5-8.5, **h** for 2070, and **i** for 2099. Grid cells are colored by local R^2 values, with dark blue indicating high model performance ($R^2 > 0.8$) and red indicating poor performance ($R^2 < 0.5$).

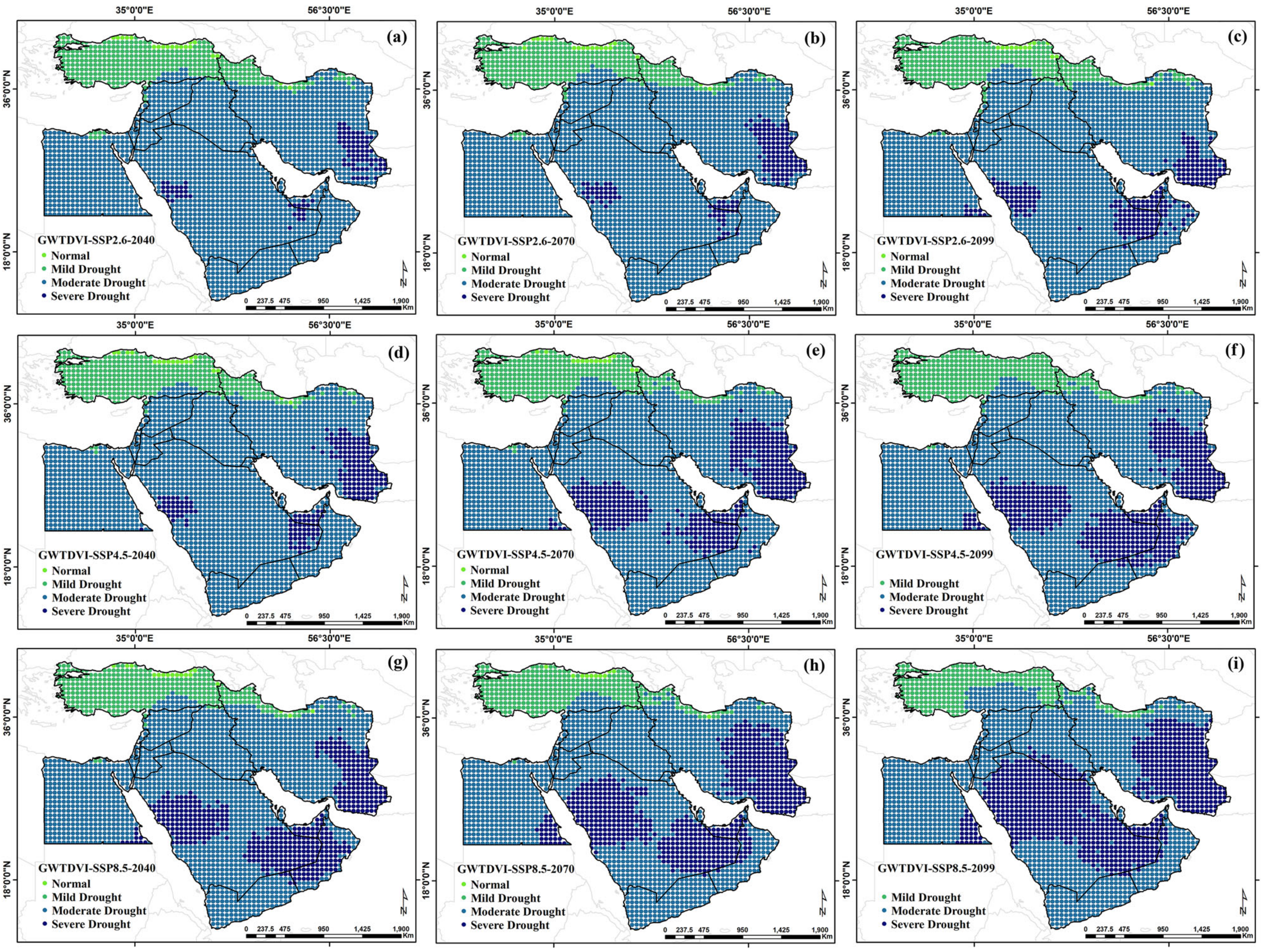

Fig. 3 | Spatiotemporal distribution of drought severity (GWTVDI) in the Middle East under future climate scenarios. a shows drought severity for the year 2040 under SSP1-2.6, (**b**) for 2070, and **c** for 2099 under the same scenario. Under SSP2-4.5, (**d**) presents drought classification for 2040, (**e**) for 2070, and **f** for 2099. Similarly, (**g**) displays drought severity for 2040 under SSP5-8.5, (**h**) for 2070, and **i** for 2099. Drought severity is categorized into four classes: normal, mild drought, moderate drought, and severe drought. Grid cells are colored accordingly, with lighter shades indicating less severe conditions and darker shades representing more intense drought. Country borders are outlined in black.

drought events are largely confined to southern and central domains with only mild to moderate intensities. This initial pattern indicates that climatic and environmental heterogeneity can, at least temporarily, act as a partial buffer for certain areas. Yet as the century advances, the increasingly pronounced signals of warming and drying progressively erode this early-stage resilience, ultimately revealing the underlying vulnerability of even ostensibly stable regions. Under the more optimistic SSP2.6 scenario (Fig. 3a–c), although mild to moderate drought affects portions of the south and center by around 2040, pockets of relative stability persist in northern areas, including Anatolia and northwestern Iran. These relatively moderate zones withstand rising temperatures and declining soil moisture well into mid-century. Nevertheless, by 2099, intensifying climatic changes within even this low-emission scenario force most of these formerly stable areas into moderate drought. Over this period, what initially appear as scattered patches of mild drought progressively coalesce under deteriorating climatic conditions into a continuous matrix of moderate to severe drought, disregarding former geographical and climatic boundaries. Thus, despite the lower emissions of SSP2.6, widespread drought becomes inevitable over time. By the end of the century, regions across southern and eastern Arabian Peninsula, as well as southwestern Iran, which had been only minimally affected by severe drought around 2040, are now more extensively impacted. In the intermediate SSP4.5 scenario (Fig. 3d–f), the intensification of climate change emerges earlier and more clearly. By mid-century, the southern and central areas experience moderate to severe drought with greater frequency and intensity, and these conditions gradually extend northward. By 2070, even regions previously characterized by relative stability face increasingly persistent drought conditions. By century's end, severe and widespread drought patterns dominate, and only some northern tracts remain under milder drought conditions. Although the rate of change under lower-emission scenarios is slower, by the long-term horizon of 2099, virtually no part of the region escapes these escalating stresses. The high-emission SSP8.5 scenario (Fig. 3g–i) represents the most extreme end-state of this continuum. Severe drought appears in many southern and central areas from the earliest decades examined, and local mitigating mechanisms such as natural vegetation cover, limited groundwater reserves, or seasonal rainfall patterns rapidly lose their effectiveness. As the century advances, this critical state becomes so pervasive that not only do near-normal conditions vanish, but even mild droughts are rarely observed. Under these circumstances, the fundamental climatic structure is changing at a rapid pace. Northern areas that once enjoyed notable resilience now face pressures comparable to those that southern regions have endured for decades. In scenarios with higher emissions (such as SSP8.5), this trend accelerates and intensifies further, rendering the control, mitigation, and management of drought by the century's end markedly more challenging than at its outset.

Discussion

The findings of this study underscore the importance of combining geographically weighted modeling and temporal trend detection for advancing drought research in the Middle East under various SSP scenarios. The newly developed GWTVDI has demonstrated superior explanatory power and predictive skill compared to the baseline TVDI model, which is limited to utilizing only the stacking-EML outputs of maximum and minimum temperature and precipitation.

Building upon these findings, compared to conventional indices such as the TVDI, the GWTVDI introduced in this study offers substantial methodological and predictive enhancements. While TVDI assumes spatial stationarity and lacks sensitivity to temporal dynamics, GWTVDI innovatively integrates Geographically Weighted Regression with the modified Mann–Kendall trend analysis, enabling it to simultaneously capture spatial heterogeneity and evolving drought trends over time. This integrated framework allows for the detection of local-scale drought anomalies and long-term climatic shifts that traditional indices like TVDI often overlook. Furthermore, GWTVDI benefits from the incorporation of advanced stacking ensemble machine learning predictions, refining the spatial and temporal resolution of input climate variables and substantially improving model accuracy. The superior performance of GWTVDI over TVDI, as demonstrated by consistently higher Adjusted R^2 values and lower AICc scores across multiple scenarios, reinforces its potential as a robust and scalable tool for adaptive drought monitoring under climate change. This advancement offers critical insights for early warning systems and proactive water management strategies in arid and vulnerable regions.

This improvement aligns with previous research emphasizing the advantages of integrating spatiotemporal features into drought prediction models. For instance[75] utilized ensemble models to improve drought vulnerability mapping, but their methods lacked the temporal dynamics that are effectively addressed by the Mann–Kendall trend analysis in this study. This significant improvement is attributable to two primary factors. First, the spatially varying coefficients within a GWR framework accommodate local heterogeneities in climatic and geographical drivers. Second, the Mann–Kendall-based trend analysis captures evolving temporal signals, addressing the non-stationary nature of drought processes. Traditional models often assume global stationarity, overlooking local nuances that can strongly influence drought propagation and severity[90]. By contrast, GWTVDI leverages spatially adaptive weights to depict how climate variables (e.g., temperature, precipitation) and geographic parameters (e.g., longitude, latitude, elevation, slope, aspect) jointly shape regional drought. This approach is consistent with findings by ref. 91, who highlighted the importance of GWR in capturing local climatic interactions. Furthermore, the incorporation of geographic parameters such as elevation and slope in GWTVDI directly addresses gaps identified in previous CMIP6-based studies, such as Song, Xia, She, Li, Hu and Hong[57], which relied primarily on bias-corrected precipitation data without integrating topographic factors.

Critically, the inclusion of temporal trends as an additional predictor in this study revealed notable improvements in model metrics, such as Adjusted R^2 and AICc, across multiple future projections. This enhancement supports the conclusions of ref. 68, who demonstrated that incorporating temporal variability substantially improves the predictive performance of climate models, particularly for extreme events such as droughts. Moreover, the Mann–Kendall-based Ti parameter provides valuable temporal insight into evolving drought conditions across the region. For instance, central and southern subregions including much of Iraq, eastern Iran, and parts of the Arabian Peninsula exhibit significant upward trends in drought severity under higher-emission scenarios such as SSP5-8.5, indicating a statistically robust increase in Ti values over time and an accelerated shift toward drier conditions. Conversely, northern and mountainous areas (e.g., Anatolia or northwestern Iran) display weaker or delayed upward trends, implying a relative buffering effect against early- or mid-century drought intensification. Nevertheless, by the latter part of the century, even these higher-latitude regions experience a more pronounced Ti signal, aligning with broader warming and drying patterns.

As with any modeling framework, GWTVDI is not immune to uncertainties. Multiple factors can affect its reliability, including the resolution and quality of remote sensing inputs, assumptions inherent in the GWR formulation, and the natural variability embedded within CMIP6 projections. In particular, consistently acquiring NDVI and LST data can be challenging in regions prone to persistent cloud cover or atmospheric disturbances. Moreover, GWR's performance relies heavily on the density and precision of spatial climate observations, indicating that areas with sparse data may necessitate additional calibration. While bias correction and downscaling techniques have been employed on CMIP6 datasets, they cannot entirely eliminate uncertainties especially under high-emission scenarios. Lastly, decisions regarding kernel bandwidth and spatial weighting in GWR can further influence the outcomes, introducing an additional layer of complexity to the modeling process.

Despite these uncertainties, the integration of ensemble machine learning approaches helps to mitigate some of these limitations by refining the prediction of key climatic variables. By leveraging stacked ensemble machine learning technique with outputs from CMIP6, this study presents a comprehensive and enhanced framework for drought forecasting. Machine learning models, such as XGBoost and CatBoost, were critical for accurately predicting key climatic variables, and their integration into the GWTVDI workflow markedly improved the accuracy and resolution of drought modeling. Coupling these ML-based predictions with GWR's locally adaptive parameter estimation has proven especially valuable for dissecting intricate patterns of drought variability at fine spatial scales. The use of GWR enhances the model's sensitivity to spatial heterogeneities, while the Mann–Kendall trend analysis addresses non-stationary dynamics in climate systems. This combination, to the best of our knowledge, delivers superior explanatory power, as evidenced by higher R^2 values and reduced AICc scores, but also identifies high-risk drought hotspots that may remain hidden in lower-resolution approaches. The results are particularly alarming under high-emission scenarios (SSP5–8.5), where extensive high-risk drought areas emerge by the end of the century. Even under moderate pathways, previously resilient regions are shown to experience worsening drought conditions over time, underscoring the cumulative impacts of progressive warming and drying trends. By integrating topographic factors, climate variables, and trend indicators, GWTVDI provides a comprehensive lens through which to understand the multifaceted interactions shaping regional drought patterns.

The enhancement offered by this framework is further underscored by the ensemble machine learning strategy. Leveraging stacking, where multiple base models including RF, XGBoost, LightGBM, CatBoost, and SVM are integrated via a meta-learner, substantially improves predictive skill, as evidenced by higher correlation coefficients and reduced RMSE compared to standalone CMIP6 projections. This outcome aligns with findings by Anaraki, Kadkhodazadeh, Morshed-Bozorgdel and Farzin[78], who showed that stacking models provide superior accuracy in projecting localized climate impacts, particularly for regions with high topographic and climatic variability. Furthermore, the enhanced precision in forecasting maximum and minimum temperatures under high-emission scenarios (e.g., SSP5-8.5) mirrors the results of Kelly et al.[92], who emphasized the critical role of advanced modeling techniques in understanding nonlinear drought intensification. In this study, by incorporating fine-scale topographic and climatic data, specific areas of heightened sensitivity were identified that might be missed by broader models, providing a crucial step for regions where local variability can momentarily reduce or amplify drought severity[93]. For example, the identification of hotspots in the central and southern regions of the Middle East under SSP4.5 and SSP5-8.5 aligns with the findings of Gerten et al.[94], who observed that even moderate climate change can progressively erode local environmental buffers. This localized analysis is crucial for regions like the Middle East, where climatic heterogeneity plays a significant role in shaping drought impacts, as highlighted by Spinoni et al.[95].

Our spatially detailed assessment of drought evolution, based on the GWTVDI, shows how warming and drying progressively change the hydrological and climatic landscape across the Middle East. The results indicate that even under lower-emission scenarios, temporary pockets of relative climate stability give way to more extensive dryness over time,

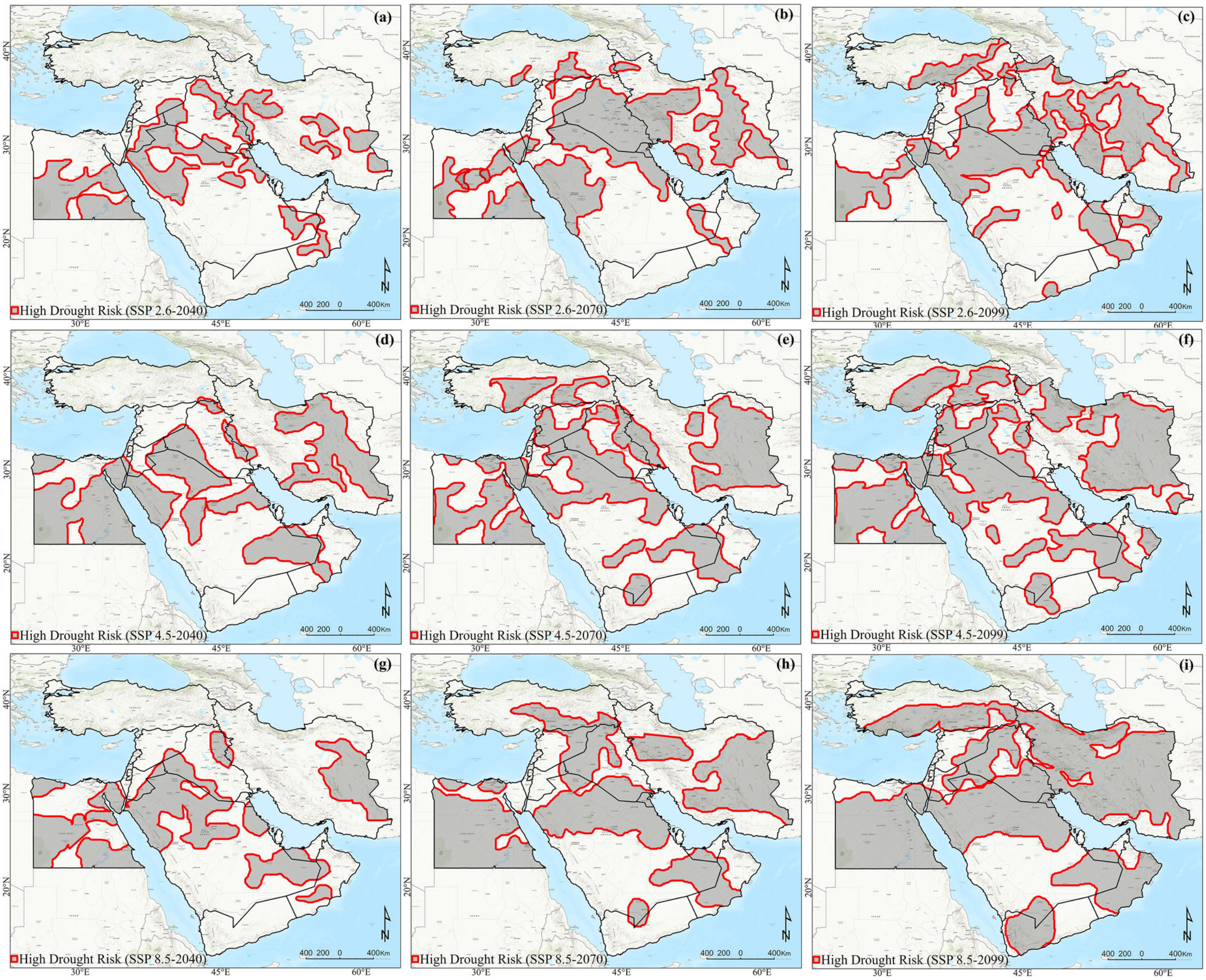

Fig. 4 | Projected high-risk drought hotspots across the Middle East under three climate scenarios. **a** shows high-risk drought areas for the year 2040 under SSP1-2.6, (**b**) for 2070, and **c** for 2099 under the same scenario. Under SSP2-4.5, (**d**) presents high-risk zones for 2040, (**e**) for 2070, and **f** for 2099. Similarly, (**g**) shows projected hotspots for 2040 under SSP5-8.5, (**h**) for 2070, and **i** for 2099. High-risk drought zones are delineated with red outlines, highlighting areas projected to experience the most severe and persistent drought conditions.

reflecting earlier findings of increasing aridity in Mediterranean and Near Eastern regions[96]. This pattern, in which maximum and minimum temperatures and precipitation anomalies gradually weaken environmental buffers, aligns with research linking extreme temperature thresholds and reduced rainfall to more frequent drought conditions[97], and it is consistent with global assessments emphasizing the vulnerability of semi-arid regions to ongoing climate shifts[98]. The temporal progression of drought risk under the Shared Socioeconomic Pathways (SSP2.6, SSP4.5, and SSP5.8) illustrates how emission levels strongly influence both the speed and extent of drought intensification.

To establish a clearer link between the continuous spatial expansion of drought signals (as shown in Fig. 3) and the discrete identification of high-risk drought zones (Fig. 4), a threshold-based classification approach was adopted. In this process, the broader GWTVDI trends representing cumulative changes in surface dryness, were refined through specific percentile-based criteria to delineate areas where climate stressors have converged to critical levels. Thus, while Fig. 3 illustrates the evolving magnitude and spatial extent of drought intensification over time, Fig. 4 presents a distilled synthesis, where locations meeting concurrent extremes in temperature sensitivity, precipitation decline, and trend significance were systematically isolated as drought hotspots. This methodological linkage ensures that high-risk zones are interpreted not as isolated anomalies, but as spatial expressions of persistent and intensifying climate-driven degradation captured through GWTVDI evolution.

In constructing our high-risk maps, we employed a multi-criteria threshold-based approach using GWTVDI outputs. Specifically, we focused on areas where the maximum and minimum temperature coefficients exceeded the 90th percentile, precipitation coefficients fell below the 10th percentile, and the Mann–Kendall-based drought trend indicator (Ti) showed a statistically significant increase. By combining these criteria, we isolated zones where warming signals, reduced precipitation, and intensifying drought trends intersect. This method aligns with previous recommendations for identifying drought hotspots[97], as it ensures that only regions experiencing pronounced climatic stressors are highlighted for further risk analysis. Moreover, the finding that high-risk zones expand markedly under SSP5-8.5 supports the conclusions of[99], who projected severe drought risks for the Middle East under high-emission scenarios. Notably, the spatially varying coefficients derived from the GWR model reveal that the identified high-risk drought zones are not driven by a single climatic factor, but rather emerge from the combined and location-specific effects of multiple climatic elements used in this study. Through GWR, we capture how local variations in temperature, precipitation, and drought's trends interact under climate change, demonstrating that these hotspots are inherently linked to the shifting climatic conditions across the region.

Indeed, the combined impact of these factors, quantified through the GWTVDI and informed by spatially varying coefficients from the GWR model, underlies the intensifying drought risk, reflecting the synergistic role of multiple climatic elements rather than the influence of any single variable. This underscores that climate change not only alters the magnitude of individual climate variables but also reshapes their interrelationships, making certain locales more vulnerable than others.

Under SSP2.6, the early decades (e.g., 2040) feature scattered high-risk locations identified by these criteria, as depicted in Fig. 4a-c. These isolated hotspots, initially limited in extent, steadily spread by mid-century (2070) and become widespread by 2099, transforming once-modest dryness into extensive high-risk zones of drought. This gradual merging of risk areas is consistent with evidence that even moderate climate change can progressively erode local resilience over multiple decades[100], and it aligns with analyses showing how incremental warming and drying can push ecosystems beyond their historical operating ranges[94]. Under the intermediate SSP4.5 scenario, the spread of high-risk zones is observed earlier and spans a broader territory. By the 2040 s (Fig. 4d–f), areas that previously maintained relative stability begin to show robust drought severity signals, limiting the time available for effective adaptation. This rapid emergence of dryness under mid-range emissions scenarios supports earlier work indicating that insufficient mitigation can lead to quick environmental decline[101], mirroring studies that underscore how intermediate warming levels still exert substantial pressure on regional water supplies[102]. In the high-emission SSP8.5 scenario, the pattern is more immediate and expansive. As early as 2040 (Fig. 4g–i), large parts of central and northern regions face intense drought risks, and by 2070 and 2099, these high-risk hotspots intensify dramatically. Such abrupt amplification resonates with findings that stronger warming signals and altered precipitation patterns can induce nonlinear and amplifying drought conditions[92], aligning with broader research demonstrating that severe emissions trajectories push arid ecosystems toward critical thresholds[103]. Local stabilizing factors, such as seasonal rainfall, groundwater stores, or vegetation, are unable to counter these compounded stressors, leading to a substantial shift in the region's climatic structure by century's end. This shift parallels predictions that severe greenhouse gas forcing can cause significant reductions in freshwater availability and agricultural viability[99]. To more clearly synthesize the emerging patterns and risks under different SSP pathways, a comparative overview reveals that while the SSP2.6 scenario initially allows for partial climatic resilience, even modest warming leads to widespread moderate droughts by the century's end. Under SSP4.5, drought intensification emerges earlier and more aggressively, with high-risk zones expanding substantially by mid-century. The SSP8.5 scenario presents the most alarming trajectory, where severe drought conditions dominate large parts of the Middle East from early decades onward, leaving almost no areas unaffected by 2099. These findings underscore that without significant mitigation efforts, regional drought resilience rapidly erodes across all scenarios, with the timing and intensity of impacts strongly dependent on the emissions pathway. Thus, the need for proactive adaptation strategies becomes more urgent as emissions increase.

These findings have profound implications for policy formulation, resource management, and agricultural planning across the Middle East. The region's well-established vulnerability to climate change, combined with the identification of high-risk drought hotspots under various SSP scenarios, highlights the urgent need for targeted interventions and adaptive strategies. These strategies include drought-tolerant crops, improved irrigation practices, strengthened water-sharing agreements, and early-warning systems that integrate real-time GWTVDI outputs to enhance preparedness and optimize resource management[22,104,105]. Such measures align with research advocating proactive and localized adaptation in regions facing complex socio-environmental challenges[106]. In addition to traditional adaptation strategies, integrating GWTVDI-based insights into multi-scale decision-making frameworks especially those enhanced by machine learning can greatly enhance drought readiness and climate resilience. The ability of GWTVDI to identify priority hotspots makes it an effective foundation for equitable water allocation, sustainable farming design, and anticipatory alert systems across vulnerable regions. The high-risk drought hotspots identified through GWTVDI, and the stacking ensemble approach hold significant importance for both national and transboundary strategies. These maps can inform collaborative efforts among Middle Eastern countries, such as Iran and Iraq, to enhance shared water governance in arid regions. Incorporating additional data, such as hydrological metrics, soil moisture, and socio-economic indicators, can further refine hotspot identification and optimize resource allocation. While early reductions in greenhouse gas emissions can mitigate the severity of future droughts, as evidenced by slower dryness progression under SSP1-2.6, accelerating changes observed in SSP4.5 and SSP5-8.5 underscore the limitations of partial mitigation efforts[102]. To advance this framework, future iterations of GWTVDI could benefit from the inclusion of high-resolution hydrological parameters, groundwater extraction records, and more granular socio-economic datasets. Such refinements would enable even more responsive and just drought-risk governance under evolving climate regimes. Since future climate patterns may deviate from historical baselines[107,108], continuous model improvements and high-resolution analyses remain critical. Integrating these projections with ecosystem and societal factors can help shape more adaptive and flexible policies. These policies may include groundwater conservation measures and early-warning drought systems to effectively address the evolving conditions in the Middle East's agricultural and hydrological sectors, fostering greater resilience and ensuring long-term sustainability.

Conclusion

This study introduced the GWTVDI, an advanced spatially adaptive index designed to improve regional drought prediction. By integrating GWR and Mann–Kendall trend analysis, GWTVDI effectively models both spatial heterogeneity and temporal evolution of drought conditions. It enables the detection of localized drought signals and long-term trends with high accuracy, addressing limitations inherent in traditional, spatially stationary indices. GWTVDI's key strength lies in its ability to dynamically adjust model coefficients based on local climatic and geographic variables, while maintaining comparability across space and time. The incorporation of satellite-derived NDVI and LST further enhances its operational utility, particularly in data-scarce regions like the Middle East. Despite these advantages, GWTVDI's performance is influenced by the quality and resolution of remote sensing data, the computational demand of GWR, and the uncertainty inherent in climate projections. Addressing these limitations particularly by incorporating additional data layers such as groundwater, soil moisture, and socio-economic indicators can improve future versions. The study also demonstrated the utility of stacking-based ensemble learning for refining climatic inputs from CMIP6 models. This hybrid strategy enhanced the spatial and temporal resolution of drought forecasts, particularly under high-emission scenarios, identifying regions at increasing risk. From a policy perspective, GWTVDI offers actionable insights for sustainable water governance, adaptive agriculture, and cross-border resource planning. Future research should aim to integrate high-resolution hydrological and socio-economic datasets into the GWTVDI framework, ultimately enhancing regional resilience to climate-induced drought risks.

Methods

The methodological framework for this study (Fig. 5) is structured into five interconnected phases: (I) Data Assembly, (II) Computation of the Temperature Vegetation Dryness Index (TVDI), (III) Historical Modeling of TVDI Using Machine Learning, (IV) Projection of Future TVDI via Stacking-Ensemble Machine Learning, and (V) Introducing the GWTVDI. This sequential design leverages multiple data sources, cutting-edge modeling approaches, and comprehensive validation strategies to enhance the spatial and temporal understanding of drought patterns.

Phase I: data assembly

This study leverages datasets from multiple sources to ensure comprehensive analysis of climate variables and drought indicators. Monthly datasets of

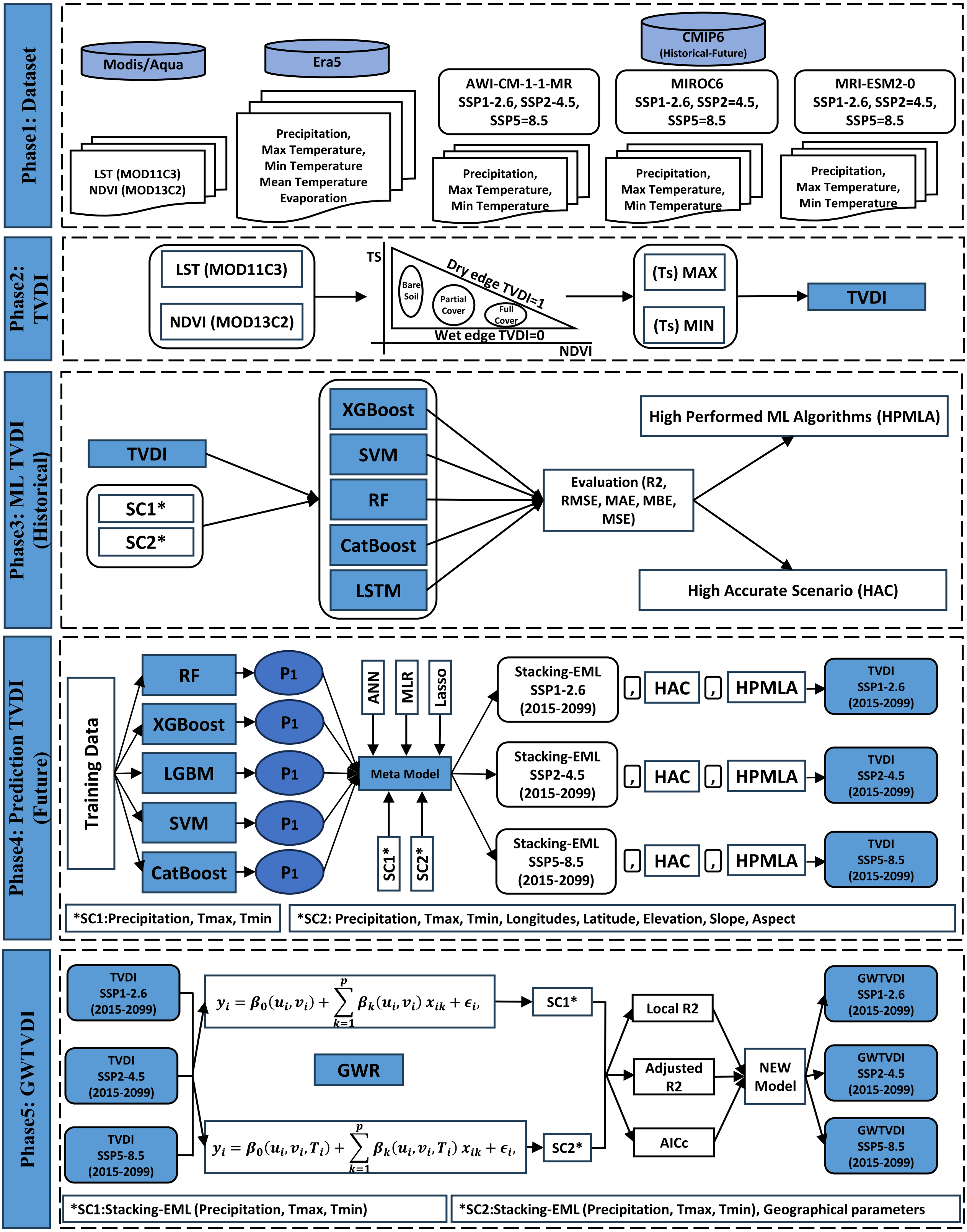

Fig. 5 | Proposed workflow for developing an enhanced stacking ensemble model for GWTVDI projections. The workflow is organized into five sequential phases. Phase I involves the assembly of satellite and climate datasets from MODIS, ERA5, and three CMIP6 models across multiple SSP scenarios. Phase II computes the Temperature Vegetation Dryness Index (TVDI) using the relationship between land surface temperature (LST) and the normalized difference vegetation index (NDVI). In Phase III, TVDI is modeled historically using five machine learning algorithms to identify the highest-performing model and input scenario. Phase IV integrates future climate projections through a Stacking Ensemble Machine Learning (Stacking-EML) framework to predict TVDI under SSP1-2.6, SSP2-4.5, and SSP5-8.5. Finally, Phase V introduces the GWTVDI by incorporating temporal trends (via Mann–Kendall) and spatial heterogeneity (via Geographically Weighted Regression), resulting in a spatially and temporally adaptive drought index.

maximum and minimum temperatures, along with precipitation, were obtained from three high-performing General Circulation Models (GCMs) within the CMIP6 framework, covering the period 2015-2100. These datasets were accessed through the Earth System Grid data distribution portal (https://cds.climate.copernicus.eu/). The CMIP6 GCMs were selected based on four key criteria: (1) a nominal spatial resolution ranging from 100 to 250 km; (2) availability of model outputs for both historical experiments and future SSP scenarios (SSP1-2.6, SSP2-4.5, and SSP5-8.5); (3) strong performance in simulating precipitation, a variable recognized for its sensitivity and greater prediction challenges compared to temperature[109]; and (4) alignment of the model's reference period with the ERA5 reanalysis dataset. Based on these criteria, three models were selected: AWI-CM-1-1-MR[110], MIROC6[111], and MRI-ESM2-0[112]. To assess their reliability, previous studies have evaluated the ability of these models to reproduce key climatic variables in the Middle East. These models have shown robust skill in capturing temperature patterns, precipitation variability, and climate extremes such as heatwaves and droughts. Compared to the broader CMIP6 ensemble, they more accurately simulate seasonal precipitation, particularly peak winter rainfall in northern subregions and reproduce long-term warming trends aligned with multi-model consensus. Their ability to reflect historical drought frequency and intensity further supports their suitability for future projections in this region[113–115].

Despite their strengths, raw GCM outputs often exhibit systematic biases, especially in mountainous or data-sparse regions[116]. To address these limitations and reconcile spatial resolution discrepancies, the model outputs were downscaled to a $0.5° \times 0.5°$ grid using co-Kriging interpolation, incorporating topographic features such as elevation, slope, and aspect to enhance spatial accuracy[117]. A two-step bias correction process, Linear Scaling followed by Quantile Mapping, was then applied to align the downscaled data with observational benchmarks[118]. Although this procedure cannot eliminate all uncertainties, it has been widely validated and is effective in reducing systematic errors and improving agreement with real-world observations[116]. Overall, these procedures ensured that the selected GCMs retained their demonstrated skill in reproducing regional climate patterns across the Middle East[119–121].

Additionally, ERA5, the fifth-generation reanalysis product from the European Centre for Medium-range Weather Forecasts, provided high-resolution data (0.1°) for maximum and minimum temperatures, precipitation, and evaporation, spanning 1995–2014 was applied. This dataset offers significant improvements over its predecessor, ERA-Interim, in terms of spatial resolution, observational coverage, representation of radiative forcing, precipitation-evaporation balance, and sea-ice dynamics[122,123]. Complementing these, satellite-derived products from the Moderate Resolution Imaging Spectroradiometer (MODIS) on Terra and Aqua were utilized, specifically the Land Surface Temperature (LST) (MOD11C3) and Normalized Difference Vegetation Index (NDVI) (MOD13C2) at 0.05° resolution. These datasets, known for their precision and extensive application in drought monitoring, provide critical insights into land surface dynamics and vegetation health, ensuring the robustness and reliability of this study's methodological framework[124]. The LST product exhibits superior spatial continuity compared to in situ data, offering higher resolution and a more suitable temporal range than LST obtained from AVHRR PAL. Frequently used in drought monitoring, this dataset provides valuable insights into land surface temperature[125]. Similarly, MODIS NDVI data is a primary resource for evaluating vegetation health and dynamics[126]. The following table provides a structured summary of the datasets used in this study (Supplementary Table 1).

Phase II: computation of TVDI

TVDI employs the spatial relationship between Land Surface Temperature (LST) and the Normalized Difference Vegetation Index (NDVI) to characterize drought conditions. Changes in surface moisture influence LST through variations in thermal properties such as heat capacity and conductivity, particularly in areas with sparse vegetation. As NDVI increases, representing denser plant cover, the LST response to soil moisture fluctuations becomes more gradual[127]. In remote sensing analyses, the relationship between LST and NDVI commonly delineates a set of reference conditions that form the conceptual foundation for TVDI derivation. Since LST responds dynamically to soil moisture variations and vegetation cover, it is the fundamental variable in TVDI computation, which relies on the LST-NDVI relationship to assess drought conditions. Unlike air temperature, which reflects atmospheric conditions, LST is directly influenced by surface energy balance, evapotranspiration, and vegetation stress, making it a more reliable indicator for assessing drought evolution[128]. Previous studies (e.g., Moran, Clarke, Inoue and Vidal[129]; Sandholt, Rasmussen and Andersen[130]) have demonstrated that these reference lines define a gradient spanning from environments with abundant soil moisture and maximum evapotranspiration to those exhibiting minimal or no evapotranspiration. The lower boundary, typically associated with higher vegetation cover and moisture availability, corresponds to regions under conditions of maximum evapotranspiration. Conversely, the upper boundary marks areas approaching zero evapotranspiration, indicative of severe moisture deficits. The intermediate range between these reference lines captures a continuum of water availability and vegetation stress, thereby enabling a nuanced characterization of drought intensity across the landscape. As NDVI rises along the horizontal axis, maximum LST diminishes, defining a "dry edge" with a negative slope derived via least squares regression. Conversely, the "wet edge" typically appears as horizontal or slightly inclined lines indicating moist conditions. Vertically, at constant NDVI, LST increases from the wet to the dry edge, reflecting escalating soil water stress. During this transition, soil moisture decreases correspondingly[128,131], and TVDI values move from 0 (extremely wet) to 1 (extremely dry) (Supplementary Fig. 1).

Although vegetation cover is limited across much of the Middle East, NDVI remains a valuable indicator for detecting subtle yet meaningful variations in vegetation stress and soil moisture. Even minimal changes in NDVI can signal localized improvements or deteriorations, particularly in areas with small-scale irrigation, riparian zones, or mountain foothills. Several studies have confirmed that NDVI-based indices can still reliably capture drought onset and progression in arid and semi-arid regions, owing to the strong coupling between surface temperature, evapotranspiration, and sparse vegetation[128,132–134]. In this study, we combine NDVI with LST to mitigate potential biases arising from low NDVI values, leveraging the contrast between 'wet edges' (denser vegetation) and 'dry edges' (bare soil). This dual approach allows small NDVI gradients to be interpreted more accurately when viewed in tandem with LST, which reflects thermal responses associated with minimal vegetation. Consequently, our TVDI formulation remains robust across both predominantly bare-soil areas and pockets of vegetation, ensuring broader applicability throughout the Middle East.

Following[130], TVDI is calculated as:

$$TVDI = \frac{LST - LST_{\min}}{LST_{\max} - LST_{\min}} \tag{1}$$

Here, $LST_{\min}$ (wet edge) and $LST_{\max}$ (dry edge) are estimated through linear regression:

$$LST_{\min} = a + b \times NDVI, LST_{\max} = c + d \times NDVI \tag{2}$$

The two components of Eq. (2), derived through linear regression analysis, represent the wet edge and dry edge, respectively. In these equations, the coefficients *a*, *b*, *c*, and *d* correspond to the parameters of the wet and dry edges. The least squares regression method was applied to identify the maximum and minimum LST values within the NDVI intervals, incremented by 0.01, using the LST-NDVI scatterplot.

Phase III: historical TVDI modeling using machine learning

The third phase employed five advanced machine learning (ML) regressors including XGBoost[135], SVM[136], RF[137], CatBoost[138], and Long short-term memory (LSTM)[139] to model and predict TVDI over a historical baseline period.

In selecting these five machine learning regressors, particular emphasis was placed on their proven capabilities in handling the nonlinearities and high-dimensionality often observed in climate datasets. Past applications in environmental modeling have repeatedly demonstrated that these algorithms not only deliver robust predictive accuracy across varied climatic regimes but also can accommodate large feature sets without substantial performance loss. Additionally, they are recognized for managing complex interactions among predictor variables (precipitation, maximum temperature, minimum temperature, longitude, latitude, elevation, slope, and aspect) and the response variable (TVDI), essential for capturing the fine-scale variability inherent to drought prediction. Beyond their predictive power, these models present distinct advantages: for instance, Random Forest offers relatively interpretable feature importance[140], XGBoost and LightGBM excel in computational efficiency through gradient-boosting frameworks[141,142], SVM maintains strong performance even with limited data[143], and CatBoost inherently manages categorical variables while mitigating overfitting[144].

Two scenarios were considered: Scenario 1 (SC1): Incorporating precipitation, maximum temperature, and minimum temperature and Scenario 2 (SC2): Extending SC1 by adding Geographical parameters (longitude, latitude, elevation, slope, aspect). These scenarios were designed to assess how topographic and spatial attributes might improve the precision of drought characterization. Each ML algorithm was optimized using a systematic hyperparameter search to achieve the highest predictive accuracy. Model performance was quantitatively assessed using multiple evaluation criteria, including the Root Mean Square Error (RMSE)[85] and the coefficient of determination (R^2). This thorough evaluation led to identifying the highest performed ML algorithms (HPMLA) and the HAC, which would be employed in subsequent phases.

To ensure a robust and reliable training process, the ML models were trained using an optimized framework. The dataset was partitioned into training (80%) and validation (20%) subsets, ensuring a balanced distribution of climate variables. A stratified fivefold cross-validation approach was applied to reduce predictive variance and improve model generalization. Additionally, hyperparameter optimization was conducted using GridSearchCV, systematically testing different parameter combinations to enhance predictive accuracy. Before final deployment, the model underwent a rigorous assessment using multiple performance indicators, such as RMSE, R^2, and MAE. By quantitatively comparing various regressors through these measures, we ensured that only the most precise and robust models were chosen for predicting TVDI. The final trained models were then tested on the independent test dataset to verify their predictive accuracy on unseen data. The best-performing model configurations were validated against historical drought events to confirm their ability to replicate observed drought variability. To further ensure the robustness of the developed GWTVDI index, a sensitivity analysis was incorporated into this phase to evaluate its response to variations in selected meteorological and geographical input variables. Regularization techniques (L1 and L2) were applied during model training to prevent excessive dependency on any single variable, thereby mitigating potential biases and enhancing the generalizability of the model. L1 regularization (L1 norm) promotes sparsity by shrinking less relevant feature weights to zero, effectively performing feature selection, whereas L2 regularization (L2 norm) reduces the magnitude of all feature weights without eliminating any, leading to a more stable model with improved generalization[145,146]. This approach effectively reduces overfitting and ensures that all input features contribute meaningfully to the drought prediction process. Furthermore, to explicitly examine the influence of geographical factors, two comparative modeling scenarios were analyzed. By assessing the variations in model performance across these scenarios, the sensitivity of GWTVDI to different input configurations was systematically evaluated. Given the observed differences in model performance, the structured evaluation incorporated into the modeling framework was deemed sufficient for capturing variations in input data, eliminating the need for a separate sensitivity analysis.

Phase IV: future TVDI projection with stacking-EML

In the fourth phase, future TVDI projections were generated by integrating climate projections from the CMIP6 scenarios with an ensemble modeling framework. Initially, five base models including RF, XGBoost, LGBM[142], SVM, and CatBoost were employed as base learners to model the climate elements (maximum temperature, minimum temperature, and precipitation) of the Middle East. A 5-fold cross-validation strategy, coupled with GridSearchCV, was employed to optimize model accuracy, and mitigate overfitting. Model performance was rigorously evaluated using RMSE and R^2. Based on these assessments, the two most accurate models were selected for further refinement. To enhance predictive accuracy, a meta-model was constructed by integrating the predictions from these two best-performing base models. This approach utilized stacking, a well-known ensemble learning technique originally proposed by Wolpert[147], which leverages the diverse strengths of multiple models. An Artificial Neural Network (ANN)[148] was integrated to develop this Stacking Ensemble Machine Learning (Stacking-EML) model, tailored to three climate scenarios including SSP1-2.6, SSP2-4.5, and SSP5-8.5, spanning the period from 2015 to 2099. Unlike traditional climate studies that rely on the ensemble mean of CMIP6 models, our approach individually utilizes selected CMIP6 models (AWI-CM-1-1-MR, MIROC6, and MRI-ESM2-0) and refines their outputs through this stacking-based ensemble learning framework. Instead of averaging out key spatial and temporal variations, this method ensures that the most reliable climate projections are incorporated while improving the precision of localized drought predictions. Finally, the Stacking-EML model, combined with the HPMLA and HAC, was employed to produce high-accuracy predictions of the TDVI under the specified conditions.

Phase V: introducing GWTVDI—integrating the modified Mann–Kendall test and geographically weighted regression

In the final methodological phase, we advance beyond conventional drought indices by introducing the GWTVDI. This innovative index not only accommodates spatial heterogeneity in climate elements relationships but also incorporates temporal trends, thus offering a comprehensive, dynamic, and spatially explicit perspective through which to evaluate drought conditions. To achieve this, we undertake three key steps: (i) Conducting a modified Mann–Kendall trend analysis of the time series, (ii) establishing a baseline GWR model, and (iii) integrating the temporal trend indicator into GWR, culminating in the enhanced GWTVDI framework.

To integrate temporal dynamics into our modeling framework, we first apply the modified Mann–Kendall test to the time series of the previously estimated TVDI across the study area. The Mann–Kendall test[149,150] is a nonparametric method widely employed to detect monotonic trends in climatological and hydrological time series[151,152]. Its robustness to non-normal data distributions and relative insensitivity to outliers make it particularly well-suited for analyzing climate-related variables[153].

For a time series ($x_1, x_2, \ldots, x_n$) of TVDI at location j, we calculate the Mann–Kendall statistic S:

$$S = \sum_{i=1}^{n-1} \sum_{j=i+1}^{n} sgn(x_j - x_i) \tag{3}$$

Where:

$$sgn(x_j - x_i) = \begin{cases} +1, & if\, x_j - x_i > 0 \\ 0, & if\, x_j - x_i = 0 \\ -1, & if\, x_j - x_i < 0 \end{cases} \tag{4}$$

Under the null hypothesis of no trend, S is approximately symmetrically distributed around zero. If no data repetitions occur, the variance

Var(S) is given by:

$$Var(s) = \frac{n(n-1)(2n+5)}{18} \tag{5}$$

In cases where repeated data values are present, a correction term is applied[150]. The standardized test statistic Z is computed as:

$$Z = \begin{cases} \frac{S-1}{\sqrt{Var(s)}} & S > 0 \\ 0 & S = 0 \\ \frac{S+1}{\sqrt{Var(s)}} & S < 0 \end{cases} \tag{6}$$

If $|Z| < Z_{\alpha/2}$ (e.g., 1.96 for a 95% confidence level), the trend is statistically significant. A positive Z indicates an increasing trend, while a negative Z suggests a decreasing trend in TVDI. We define the obtained Z-score for each pixel as T_i, a temporal trend indicator representing how drought conditions evolve over time at each location.

Geographically Weighted Regression (GWR) extends traditional regression models by allowing local rather than global parameter estimates, thus capturing spatial heterogeneity[91]. Initially, we implement a baseline GWR model to characterize the spatial variability in TVDI as a function of climatic predictors such as maximum temperature, minimum temperature, and precipitation. In this baseline formulation:

$$y_i = \beta_0(u_i, v_i) + \sum_{k=1}^{p} \beta_k(u_i, v_i)\, x_{ik} + \epsilon_i, \tag{7}$$

Where y_i is the TVDI at location i, x_{ik} are the independent climatic variables, and $\beta_k(u_i, v_i)$ are spatially varying coefficients estimated by weighting observations based on their proximity to i.

In this study, local weighting within the GWR framework is determined by a kernel function (Gaussian). Under this approach, grid points that lie closer to location i receive higher weights. The kernel's bandwidth is also selected via automated procedures such as minimizing the AICc to strike an optimal balance between local fit and model stability. Given the inherently local and data-driven nature of GWR, the coefficients $\beta_k(u_i, v_i)$ are calculated independently for each location rather than remaining fixed across the entire region. As a result, the relative contribution of each variable in different Middle Eastern climates is dynamic. Whenever regional climatic conditions, topography, or local data vary, the associated coefficients and weights for each variable adjust accordingly. This adaptability accommodates ecological and climatic distinctions across different areas and thereby improves the accuracy of local drought prediction patterns.

A key innovation of this study is the integration of the temporal trend indicator T_i derived from the Mann–Kendall analysis into the GWR framework. By incorporating T_i,we effectively transform the GWR model into a spatiotemporal modeling structure, capturing how both spatial heterogeneity and temporal evolution jointly influence drought patterns. The extended model is formulated as:

$$y_i = \beta_0(u_i, v_i, T_i) + \sum_{k=1}^{p} \beta_k(u_i, v_i,\ T_i)\, x_{ik} + \epsilon_i, \tag{8}$$

Where coefficients further decomposed as:

$$\beta_k(u_i, v_i, T_i) = \beta_k^0(u_i, v_i) + \beta_k^T(u_i, v_i)\, T_i, \tag{9}$$

$$\beta_0(u_i, v_i, T_i) = \beta_0^0(u_i, v_i) + \beta_0^T(u_i, v_i)\, T_i. \tag{10}$$

In this refined specification, $\beta_k^0(u_i, v_i)$ captures the baseline spatial influence of each climatic variable on TVDI, while $\beta_k^T(u_i, v_i)$ quantifies how temporal trends modulate this influence. Thus, a positive $\beta_k^T(u_i, v_i)$ suggests that as drought severity intensifies over time (positive T_i), the influence of the associated climatic variable x_{ik} on TVDI grows stronger, and vice versa. By incorporating T_i and geographic parameters (e.g., longitude, latitude, elevation, slope, aspect) into the GWR model, we derive the Geographically Weighted Temperature Vegetation Dryness Index (GWTVDI). This geographically sensitive approach, aligned with the method proposed by ref. 88, ultimately advances drought prediction accuracy and provides a refined understanding of drought variability.

Just like TVDI, the GWTVDI values range between 0 (extremely wet) and 1 (extremely dry). Therefore, we follow a thresholding approach similar to TVDI for determining when a location is considered to be in drought conditions. Specifically, GWTVDI values closer to 1 indicate increasing levels of surface dryness, making it feasible to categorize drought intensity (e.g., moderate, severe, extreme) by comparing local GWTVDI against established percentile or seasonal reference levels. By combining the GWTVDI equation with the Mann–Kendall-based trend analysis, we capture both short-term dryness and long-term changes in climate variables. Persistently elevated GWTVDI values, especially above the typical historical or seasonal thresholds, are deemed indicative of abnormal climate extremes (i.e., drought events), rather than merely reflecting a continuously dry environment. This threshold mechanism ensures that GWTVDI retains the practical clarity of TVDI while incorporating spatial heterogeneity and temporal evolution through GWR.

To maximize the performance of the base models, an extensive grid search with cross-validation was conducted to identify the most effective hyperparameter configurations. This method involved systematically exploring various parameter combinations within predefined ranges, drawing inspiration from prior studies research[18,154]. Each hyperparameter set was evaluated using a tenfold cross-validation (CV) strategy alongside performance metrics such as RMSE and R^2. This approach allowed for repeated validation across different data subsets, effectively reducing variance and minimizing the potential for overfitting. Through this comprehensive search, we determined the optimal hyperparameters for each base model. These optimized models were then incorporated as base learners within the stacking ensemble framework. Detailed information on the specific hyperparameters and their tested values for each base model is provided in Supplementary Table 2.

Study area

The Middle East (Fig. 6a), geographically covering about 6,928,000 km², consists of sixteen countries with a population level reaching ~320 million. Most of this region is hot and dry or semi-dry, with extensive deserts where temperatures can exceed 50 °C during the summer months across vast areas of the Arabian Peninsula and drop below zero during winter in mountainous geographical formations, such as Turkey and northern Iran[155]. Despite this aridness, northeastern Iraq, western Syria, northwestern Iran, and Lebanon appear to have relatively higher levels of precipitation that support grasslands, forests, and cultivated lands[156]. Rainfall is very seasonal, peaking between November and April through synoptic storms, with certain areas like the Caspian Sea coast receiving 1800 mm, providing critical water resources to reduce drought pressures[157]. As illustrated in Fig. 6b, the distribution of annual precipitation across the Middle East exhibits marked regional variability. The most substantial rainfall totals occur along the eastern Mediterranean coast, the western slopes of the Zagros Mountains in Iran, the southern coastline of the Caspian Sea, and the most part of Turkey. These areas benefit from orographic uplift and synoptic weather systems especially during the colder months that enhance precipitation along mountainous terrain. In contrast, extensive areas of the Middle East including the Syrian Desert, the central and southern Arabian Peninsula, and interior parts of Egypt and Iran receive very little rainfall annually. Although drylands are primarily characterized by barren land and rangelands, favorable climatic conditions support agriculture and vegetation essential to the environment and people. These ecosystems underscore the resiliency of the region and offer opportunities for sustainable adaptations to climate change.

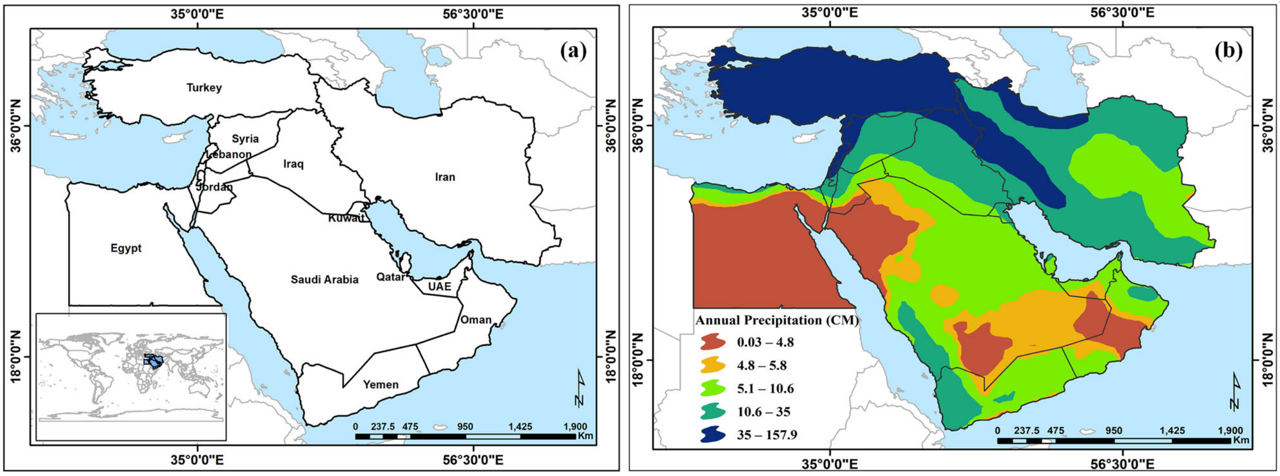

Fig. 6 | Geographical extent and annual precipitation in the Middle East. **a** Country boundaries of the Middle East are shown, covering sixteen countries. An inset highlights the location of the study area in the global context. **b** Spatial distribution of average annual precipitation across the region, categorized from 0.03 cm (red) to 157.9 cm (dark blue). High precipitation occurs along the eastern Mediterranean coast, the Zagros Mountains, and the southern Caspian Sea. In contrast, low-rainfall zones dominate the Arabian Peninsula and central Egypt. Country borders are shown in black and water bodies in light blue.

However, the Middle East is also widely recognized as one of the most vulnerable regions to future climate change. Multiple studies project that rising temperatures and shifting precipitation regimes will intensify drought episodes, exacerbate water scarcity, and potentially challenge agricultural sustainability[53]. Under more extreme emission pathways (e.g., SSP5-8.5), rising temperatures may intensify existing heat stress in nations already contending with insufficient water supplies. Additionally, socioeconomic pressures such as rapid population expansion and transboundary water dependencies further compound the region's vulnerability to climatic shocks. Within this context, analyzing drought patterns across the Middle East emerges as both a scientific imperative and a pivotal step for advancing policy development, water governance, and broader regional collaboration[158].

Data availability

All data supporting the findings of this study are publicly available. The CMIP6 general circulation model (GCM) outputs and ERA5 reanalysis datasets were obtained from the Copernicus Climate Data Store (https://cds.climate.copernicus.eu/). MODIS remote sensing products, including land surface temperature (LST) and normalized difference vegetation index (NDVI), were downloaded from the NASA LAADS DAAC platform (https://ladsweb.modaps.eosdis.nasa.gov/). Digital Elevation Model (DEM) data were acquired via OpenTopography (https://portal.opentopography.org/). The source data used to generate all figures and charts in this study are available on Figshare: https://doi.org/10.6084/m9.figshare.28907981.v1.

Code availability

All codes necessary for reproducibility of the results are available at https://figshare.com/articles/dataset/Codes/28915130.

Received: 16 January 2025; Accepted: 6 May 2025;
Published online: 16 May 2025

References

1. Fawzy, S., Osman, A. I., Doran, J. & Rooney, D. W. Strategies for mitigation of climate change: a review. *Environ. Chem. Lett.* **18**, 2069–2094 (2020).
2. Yousefi, H., Ahani, A., Moridi, A. & Razavi, S. The future of droughts in Iran according to CMIP6 projections. *Hydrol. Sci. J.* **69**, 951–970 (2024).
3. Ouarda, T. B. & Charron, C. Changes in the distribution of hydro-climatic extremes in a non-stationary framework. *Sci. Rep.* **9**, 8104 (2019).
4. Raymond, C. et al. Understanding and managing connected extreme events. *Nat. Clim. change* **10**, 611–621 (2020).
5. Shetty, S., Umesh, P. & Shetty, A. The effectiveness of machine learning-based multi-model ensemble predictions of CMIP6 in Western Ghats of India. *Int. J. Climatol.* **43**, 5029–5054 (2023).
6. Zhang, P., Lu, J. & Chen, X. Machine-learning ensembled CMIP6 projection reveals socio-economic pathways will aggravate global warming and precipitation extreme. *Hydrol. Earth Syst. Sci. Discuss.* **2022**, 1–40 (2022).
7. Cook, B. I., Ault, T. R. & Smerdon, J. E. Unprecedented 21st century drought risk in the American Southwest and Central Plains. *Sci. Adv.* **1**, e1400082 (2015).
8. Gonzalez, R. et al. Water budget analysis in arid regions, application to the United Arab Emirates. *Water* **8**, 415 (2016).
9. Khosravi, Y., Homayouni, S. & Ouarda, T. B. Spatio-temporal evaluation of MODIS temperature vegetation dryness index in the Middle East. *Ecol. Inform.* **84**, 102894 (2024).
10. Skoulikaris, C., Makris, C., Katirtzidou, M., Baltikas, V. & Krestenitis, Y. Assessing the vulnerability of a deltaic environment due to climate change impact on surface and coastal waters: The case of Nestos River (Greece). *Environ. Model. Assess.* **26**, 459–486 (2021).
11. Ouarda, T. B. et al. Evolution of the rainfall regime in the United Arab Emirates. *J. Hydrol.* **514**, 258–270 (2014).
12. Stocker, T. Climate change 2013: the physical science basis: Working Group I contribution to the Fifth assessment report of the Intergovernmental Panel on Climate Change (Cambridge University Press, 2014).
13. Nagarajan, R. *Drought Assessment* (Springer Science & Business Media, 2010).
14. Hamdi, Y., Chebana, F. & Ouarda, T. B. Bivariate drought frequency analysis in the Medjerda River Basin, Tunisia. *J. Civil Environ. Eng.* **6** (2016).
15. Jiang, Z. et al. Can ensemble machine learning be used to predict the groundwater level dynamics of farmland under future climate: a 10-year study on Huaibei Plain. *Environ. Sci. Pollut. Res.* **29**, 44653–44667 (2022).
16. Eddamiri, S. et al. Modeling the impact of climate change on wheat yield in Morocco based on stacked ensemble learning. *Model. Earth Syst. Environ.* 1–21 (2024).
17. Zhao, X. et al. Projections of meteorological drought based on CMIP6 multi-model ensemble: a case study of Henan Province, China. *J. Contam. Hydrol.* **243**, 103887 (2021).

18. Ali, M. G., Younes, K., Esmaeil, A. & Fatemeh, T. Assessment of geostatistical methods for spatial analysis of SPI and EDI drought indices. *World Appl. Sci. J.* **15**, 474–482 (2011).
19. Masson-Delmotte, V. et al. IPCC, 2021: Summary for policymakers. in: Climate change 2021: The physical science basis. contribution of working group i to the sixth assessment report of the intergovernmental panel on climate change (2021).
20. Patel, R. & Patel, A. Evaluating the impact of climate change on drought risk in semi-arid region using GIS technique. *Results Eng.* **21**, 101957 (2024).
21. Laz, O. U., Rahman, A. & Ouarda, T. B. Compound heatwave and drought hotspots and their trends in Southeast Australia. *Nat. Hazards* **119**, 357–386 (2023).
22. Lesk, C., Rowhani, P. & Ramankutty, N. Influence of extreme weather disasters on global crop production. *Nature* **529**, 84–87 (2016).
23. Xu, X. et al. Unleashing the power of machine learning and remote sensing for robust seasonal drought monitoring: a stacking ensemble approach. *J. Hydrol.* **634**, 131102 (2024).
24. Modarres, R. & Ouarda, T. B. Modeling the relationship between climate oscillations and drought by a multivariate GARCH model. *Water Resour. Res.* **50**, 601–618 (2014).
25. Mollick, T., Hashmi, G. & Sabuj, S. R. A perceptible stacking ensemble model for air temperature prediction in a tropical climate zone. *Discov. Environ.* **1**, 15 (2023).
26. Lee, T., Modarres, R. & Ouarda, T. B. Data-based analysis of bivariate copula tail dependence for drought duration and severity. *Hydrol. Process.* **27**, 1454–1463 (2013).
27. Palmer, W. C. Meteorological drought, Vol. 30 (US Department of Commerce, Weather Bureau, 1965).
28. McKee, T. B., Doesken, N. J. & Kleist, J. In: *Proc. 8th Conference on Applied Climatology* 17 179−183 (Boston, 1993).
29. Vicente-Serrano, S. M., Beguería, S. & López-Moreno, J. I. A multiscalar drought index sensitive to global warming: the standardized precipitation evapotranspiration index. *J. Clim.* **23**, 1696–1718 (2010).
30. Wells, N., Goddard, S. & Hayes, M. J. A self-calibrating Palmer drought severity index. *J. Clim.* **17**, 2335–2351 (2004).
31. Zhao, D. et al. Are the traditional large-scale drought indices suitable for shallow water wetlands? An example in the Everglades. *J. Environ. Manag.* **198**, 240–247 (2017).
32. Prodhan, F. A., Zhang, J., Bai, Y., Sharma, T. P. P. & Koju, U. A. Monitoring of drought condition and risk in Bangladesh combined data from satellite and ground meteorological observations. *IEEE Access* **8**, 93264–93282 (2020).
33. Hoffmann, D., Gallant, A. J. & Arblaster, J. M. Uncertainties in drought from index and data selection. *J. Geophys. Res.: Atmos.* **125**, e2019JD031946 (2020).
34. Singh, G. R., Dhanya, C. & Chakravorty, A. A robust drought index accounting changing precipitation characteristics. *Water Resour. Res.* **57**, e2020WR029496 (2021).
35. Liu, Y. et al. Sensitivity analysis of standardization procedures in drought indices to varied input data selections. *J. Hydrol.* **538**, 817–830 (2016).
36. Shrestha, A. et al. Regional climatological drought: an assessment using high-resolution data. *Hydrology* **7**, 33 (2020).
37. Hussain, Z. et al. CORDEX Ensemble-based drought projections for Sindh Province of Pakistan under climate change. *J. Water Clim. Change* **15**, 5501–5517 (2024).
38. Gebrechorkos, S. H. et al. Global high-resolution drought indices for 1981–2022. *Earth Syst. Sci. Data Discuss.* **2023**, 1–28 (2023).
39. Fragaszy, S. R. et al. Drought monitoring in the Middle East and North Africa (MENA) region: participatory engagement to inform early warning systems. *Bull. Am. Meteorol. Soc.* **101**, E1148–E1173 (2020).
40. Kenawy, A. E., Al-Awadhi, T., Abdullah, M., Ostermann, F. O. & Abulibdeh, A. A Multidecadal assessment of drought intensification in the Middle East and North Africa: the role of global warming and rainfall deficit. *Earth Syst. Environ.* 1–20 (2025).
41. Barlow, M. et al. A review of drought in the Middle East and southwest Asia. *J. Clim.* **29**, 8547–8574 (2016).
42. Peres, D. J. et al. (Copernicus Meetings, 2024).
43. Xiong, J., Guo, S., Kinouchi, T. & Anjaneyulu, R. Emerging trends and spatial shifts of drought potential across global river basins. *J. Environ. Manag.* **352**, 120093 (2024).
44. El Kenawy, A. M., Vicente-Serrano, S. M., Murphy, C. & Gimeno, L. 11 1140658 (Frontiers Media SA, 2023).
45. Mishra, A. K. & Singh, V. P. Drought modeling–a review. *J. Hydrol.* **403**, 157–175 (2011).
46. Shashikanth, K. et al. Comparing statistically downscaled simulations of Indian monsoon at different spatial resolutions. *J. Hydrol.* **519**, 3163–3177 (2014).
47. Yang, Y., Bai, L., Wang, B., Wu, J. & Fu, S. Reliability of the global climate models during 1961–1999 in arid and semiarid regions of China. *Sci. Total Environ.* **667**, 271–286 (2019).
48. Bosso, F. Improving sub-seasonal drought forecasting via machine learning to leverage climate data at different spatial scales. (2021).
49. Giuliani, M., Bosso, F., Bertini, C., Solomatine, D. & van Andel, S. J. (Copernicus Meetings, 2024).
50. Arshad, S., Kazmi, J. H., Prodhan, F. A. & Mohammed, S. Exploring dynamic response of agrometeorological droughts towards winter wheat yield loss risk using machine learning approach at a regional scale in Pakistan. *Field Crops Res.* **302**, 109057 (2023).
51. Bauer, P., Thorpe, A. & Brunet, G. The quiet revolution of numerical weather prediction. *Nature* **525**, 47–55 (2015).
52. Pinheiro, E. & Ouarda, T. B. Short-lead seasonal precipitation forecast in northeastern Brazil using an ensemble of artificial neural networks. *Sci. Rep.* **13**, 20429 (2023).
53. Tabari, H. & Willems, P. More prolonged droughts by the end of the century in the Middle East. *Environ. Res. Lett.* **13**, 104005 (2018).
54. Pinheiro, E. & Ouarda, T. B. An interpretable machine learning model for seasonal precipitation forecasting. *Commun. Earth Environ.* **6**, 1–14 (2025).
55. Prodhan, F. A., Zhang, J., Hasan, S. S., Sharma, T. P. P. & Mohana, H. P. A review of machine learning methods for drought hazard monitoring and forecasting: current research trends, challenges, and future research directions. *Environ. Model. Softw.* **149**, 105327 (2022).
56. Meinshausen, M. et al. The shared socio-economic pathway (SSP) greenhouse gas concentrations and their extensions to 2500. *Geosci. Model Dev.* **13**, 3571–3605 (2020).
57. Song, Z. et al. Assessment of meteorological drought change in the 21st century based on CMIP6 multi-model ensemble projections over mainland China. *J. Hydrol.* **601**, 126643 (2021).
58. Zhai, J. et al. Future drought characteristics through a multi-model ensemble from CMIP6 over South Asia. *Atmos. Res.* **246**, 105111 (2020).
59. Yan, Y. et al. Projection of future extreme precipitation in China based on the CMIP6 from a machine learning perspective. *Remote Sens.* **14**, 4033 (2022).
60. Dey, A., Sahoo, D. P., Kumar, R. & Remesan, R. A multimodel ensemble machine learning approach for CMIP6 climate model projections in an Indian River basin. *Int. J. Climatol.* **42**, 9215–9236 (2022).
61. Prodhan, F. A. et al. Projection of future drought and its impact on simulated crop yield over South Asia using ensemble machine learning approach. *Sci. Total Environ.* **807**, 151029 (2022).
62. Zhang, R. Second International Conference on Networks, Multimedia and Information Technology (NMITCON) 1-5 (IEEE, 2024).

63. Mokhtar, A. et al. Estimation of SPEI meteorological drought using machine learning algorithms. *IEEe Access* **9**, 65503–65523 (2021).
64. Kim, K., Kim, B. & Han, K.-Y. Performance evaluation of effective drought prediction using machine learning. *J. Korean Soc. Hazard Mitig.* **21**, 195–204 (2021).
65. Gu, J., Liu, S., Zhou, Z., Chalov, S. R. & Zhuang, Q. A stacking ensemble learning model for monthly rainfall prediction in the Taihu Basin, China. *Water* **14**, 492 (2022).
66. Jiao, W., Tian, C., Chang, Q., Novick, K. A. & Wang, L. A new multi-sensor integrated index for drought monitoring. *Agric. For. Meteorol.* **268**, 74–85 (2019).
67. Neeti, N., Murali, C. A., Chowdary, V., Rao, N. & Kesarwani, M. Integrated meteorological drought monitoring framework using multi-sensor and multi-temporal earth observation datasets and machine learning algorithms: a case study of central India. *J. Hydrol.* **601**, 126638 (2021).
68. Zhao, L., Lu, S. & Qi, D. Improvement of maximum air temperature forecasts using a stacking ensemble technique. *Atmosphere* **14**, 600 (2023).
69. Fu, Y., Zhuang, H., Shen, X. & Li, W. Assessment and prediction of regional climate based on a multimodel ensemble machine learning method. *Clim. Dyn.* **61**, 4139–4158 (2023).
70. Jaiswal, P. G. et al. In: Proc. 6th International Conference on Information Systems and Computer Networks (ISCON) 1–6 (IEEE, 2023).
71. Jose, D. M., Vincent, A. M. & Dwarakish, G. S. Improving multiple model ensemble predictions of daily precipitation and temperature through machine learning techniques. *Sci. Rep.* **12**, 4678 (2022).
72. Wang, S., Wu, Y., Li, R. & Wang, X. Remote sensing-based retrieval of soil moisture content using stacking ensemble learning models. *Land Degrad. Dev.* **34**, 911–925 (2023).
73. Tahmouresi, M. S., Niksokhan, M. H. & Ehsani, A. H. Enhancing spatial resolution of satellite soil moisture data through stacking ensemble learning techniques. *Sci. Rep.* **14**, 25454 (2024).
74. Granata, F., Di Nunno, F., Najafzadeh, M. & Demir, I. A stacked machine learning algorithm for multi-step ahead prediction of soil moisture. *Hydrology* **10**, 1 (2022).
75. Arabameri, A. et al. Drought risk assessment: integrating meteorological, hydrological, agricultural and socio-economic factors using ensemble models and geospatial techniques. *Geocarto Int.* **37**, 6087–6115 (2022).
76. Cheng, Y. et al. In: *Proc. IEEE International Geoscience and Remote Sensing Symposium IGARSS* 6984-6987 (IEEE, 2021).
77. Adede, C., Oboko, R., Wagacha, P. W. & Atzberger, C. Model ensembles of artificial neural networks and support vector regression for improved accuracy in the prediction of vegetation conditions and droughts in four northern Kenya counties. *ISPRS Int. J. Geo-Inf.* **8**, 562 (2019).
78. Anaraki, M. V., Kadkhodazadeh, M., Morshed-Bozorgdel, A. & Farzin, S. Predicting rainfall response to climate change and uncertainty analysis: Introducing a novel downscaling CMIP6 models technique based on the stacking ensemble machine learning. *J. Water Clim. Change* **14**, 3671–3691 (2023).
79. Raza, O., Memon, M., Bhatti, S. & Pathan, N. Drought prediction with raw satellite imagery and ensemble supervised machine learning. *Rev. Environ. Earth Sci.* **8**, 1–7 (2021).
80. Hanadé Houmma, I., El Mansouri, L., Gadal, S., Garba, M. & Hadria, R. Modelling agricultural drought: a review of latest advances in big data technologies. *Geomat., Nat. Hazards Risk* **13**, 2737–2776 (2022).
81. Boldini, D., Grisoni, F., Kuhn, D., Friedrich, L. & Sieber, S. A. Practical guidelines for the use of gradient boosting for molecular property prediction. *J. Cheminform.* **15**, 73 (2023).
82. Liu, X. et al. Splitting and length of years for improving tree-based models to predict reference crop evapotranspiration in the humid regions of China. *Water* **13**, 3478 (2021).
83. Ouarda, T. B. & Shu, C. Regional low-flow frequency analysis using single and ensemble artificial neural networks. *Water Resour. Res.* **45** (2009).
84. Haykin, S. *Neural Networks: a Comprehensive Foundation* (Prentice Hall PTR, 1998).
85. Draper, N. *Applied Regression Analysis* (McGraw-Hill. Inc, 1998).
86. Tibshirani, R. Regression shrinkage and selection via the lasso. *J. R. Stat. Soc. Ser. B: Stat. Methodol.* **58**, 267–288 (1996).
87. Hammami, D., Lee, T. S., Ouarda, T. B. & Lee, J. Predictor selection for downscaling GCM data with LASSO. *J. Geophys. Res. Atmos.* **117** (2012).
88. Khosravi, Y., Homayouni, S. & St-Hilaire, A. An integrated dryness index based on geographically weighted regression and satellite earth observations. *Sci. Total Environ.* **911**, 168807 (2024).
89. Akaike, H. in Selected papers of hirotugu akaike 199-213 (Springer, 1998).
90. Tran, H. T., Campbell, J. B., Tran, T. D. & Tran, H. T. Monitoring drought vulnerability using multispectral indices observed from sequential remote sensing (Case Study: Tuy Phong, Binh Thuan, Vietnam). *GIScience Remote Sens.* **54**, 167–184 (2017).
91. Fotheringham, A. S., Brunsdon, C. & Charlton, M. Geographically weighted regression. *Sage Handb. Spat. Anal.* **1**, 243–254 (2009).
92. Kelley, C. P., Mohtadi, S., Cane, M. A., Seager, R. & Kushnir, Y. Climate change in the Fertile Crescent and implications of the recent Syrian drought. *Proc. Natl. Acad. Sci.* **112**, 3241–3246 (2015).
93. Boulanger, J.-P., Carril, A. F. & Sanchez, E. CLARIS-La Plata Basin: regional hydroclimate variability, uncertainties and climate change scenarios. *Clim. Res.* **68**, 93–94 (2016).
94. Gerten, D. et al. Feeding ten billion people is possible within four terrestrial planetary boundaries. *Nat. Sustain.* **3**, 200–208 (2020).
95. Spinoni, J., Vogt, J. V., Naumann, G., Barbosa, P. & Dosio, A. Will drought events become more frequent and severe in Europe? (2018).
96. Cook, B. I., Anchukaitis, K. J., Touchan, R., Meko, D. M. & Cook, E. R. Spatiotemporal drought variability in the Mediterranean over the last 900 years. *J. Geophys. Res. Atmos.* **121**, 2060–2074 (2016).
97. Touma, D., Ashfaq, M., Nayak, M. A., Kao, S.-C. & Diffenbaugh, N. S. A multi-model and multi-index evaluation of drought characteristics in the 21st century. *J. Hydrol.* **526**, 196–207 (2015).
98. Huang, J., Yu, H., Guan, X., Wang, G. & Guo, R. Accelerated dryland expansion under climate change. *Nat. Clim. change* **6**, 166–171 (2016).
99. Schewe, J. et al. Multimodel assessment of water scarcity under climate change. *Proc. Natl. Acad. Sci.* **111**, 3245–3250 (2014).
100. Lorenz, D. J., DeWeaver, E. T. & Vimont, D. J. Evaporation change and global warming: the role of net radiation and relative humidity. *J. Geophys. Res. Atmos.* **115** (2010).
101. Evans, J. P. 21st century climate change in the Middle East. *Clim. change* **92**, 417–432 (2009).
102. Dai, A. Increasing drought under global warming in observations and models. *Nat. Clim. change* **3**, 52–58 (2013).
103. Seneviratne, S. et al. Changes in climate extremes and their impacts on the natural physical environment. (2012).
104. AghaKouchak, A. et al. Remote sensing of drought: Progress, challenges and opportunities. *Rev. Geophys.* **53**, 452–480 (2015).
105. Wada, Y., Van Beek, L. P., Wanders, N. & Bierkens, M. F. Human water consumption intensifies hydrological drought worldwide. *Environ. Res. Lett.* **8**, 034036 (2013).
106. Diffenbaugh, N. S. & Burke, M. Global warming has increased global economic inequality. *Proc. Natl Acad. Sci.* **116**, 9808–9813 (2019).
107. Trenberth, K. E., Fasullo, J. T., Branstator, G. & Phillips, A. S. Seasonal aspects of the recent pause in surface warming. *Nat. Clim. Change* **4**, 911–916 (2014).

108. Masson-Delmotte, V. et al. Climate change 2021: the physical science basis. *Contribution working group I sixth Assess. Rep. intergovernmental panel Clim. change* **2**, 2391 (2021).
109. Yılmaz, B., Aras, E. & Nacar, S. A CMIP6-ensemble-based evaluation of precipitation and temperature projections. *Theoret. Appl. Climatol.* 1–25 (2024).
110. Semmler, T. et al. Simulations for CMIP6 with the AWI climate model AWI-CM-1-1. *J. Adv. Model. Earth Syst.* **12**, e2019MS002009 (2020).
111. Shiogama, H. MIROC MIROC6 model output prepared for CMIP6 DAMIP hist-CO_2 (2019).
112. Yukimoto, S. et al. The Meteorological Research Institute Earth System Model version 2.0, MRI-ESM2. 0: description and basic evaluation of the physical component. *J. Meteorol. Soc. Jpn. Ser. II* **97**, 931–965 (2019).
113. Mukheef, R. A., Hassan, W. H. & Alquzweeni, S. Projections of temperature and precipitation trends using CMhyd under CMIP6 scenarios: a case study of Iraq's Middle and West. *Atmos. Res.* **306**, 107470 (2024).
114. Yazdandoost, F., Moradian, S., Izadi, A. & Aghakouchak, A. Evaluation of CMIP6 precipitation simulations across different climatic zones: uncertainty and model intercomparison. *Atmos. Res.* **250**, 105369 (2021).
115. Shi, J., Stepanek, C., Sein, D., Streffing, J. & Lohmann, G. East Asian summer precipitation in AWI-CM3: comparison with observations and CMIP6 models. *Int. J. Climatol.* **43**, 4083–4098 (2023).
116. Gao, W. et al. A deconfounding approach to climate model bias correction. *arXiv preprint arXiv:2408.12063* (2024).
117. Khosravi, Y. & Balyani, S. Spatial modeling of mean annual temperature in Iran: comparing cokriging and geographically weighted regression. *Environ. Model. Assess.* **24**, 341–354 (2019).
118. Enayati, M., Bozorg-Haddad, O., Bazrafshan, J., Hejabi, S. & Chu, X. Bias correction capabilities of quantile mapping methods for rainfall and temperature variables. *J. Water Clim. Change* **12**, 401–419 (2021).
119. Shiru, M. S. & Chung, E.-S. Performance evaluation of CMIP6 global climate models for selecting models for climate projection over Nigeria. *Theor. Appl. Climatol.* **146**, 599–615 (2021).
120. Hamed, M. M., Nashwan, M. S. & Shahid, S. A novel selection method of CMIP6 GCMs for robust climate projection. *Int. J. Climatol.* **42**, 4258–4272 (2022).
121. Agyekum, J. et al. Extreme temperature indices over the Volta Basin: CMIP6 model evaluation. *Clim. Dyn.* **61**, 203–228 (2023).
122. Hersbach, H. et al. The ERA5 global reanalysis. *Q. J. R. Meteorol. Soc.* **146**, 1999–2049 (2020).
123. Amjad, M., Yilmaz, M. T., Yucel, I. & Yilmaz, K. K. Performance evaluation of satellite-and model-based precipitation products over varying climate and complex topography. *J. Hydrol.* **584**, 124707 (2020).
124. Cai, G., Du, M. & Liu, Y. in Computer and computing technologies in agriculture IV: 4th IFIP TC 12 Conference, CCTA 2010, Nanchang, China, October 22-25, 2010, Selected Papers, Part II 4 243-251 (Springer, 2011).
125. Zhao, X. et al. Drought monitoring over Yellow River basin from 2003–2019 using reconstructed MODIS land surface temperature in Google Earth Engine. *Remote Sens.* **13**, 3748 (2021).
126. Ndungu, L. et al. Application of MODIS NDVI for monitoring Kenyan rangelands through a web based decision support tool. *Front. Environ. Sci.* **7**, 475659 (2019).
127. Uddin, M. J. & Mondal, C. Effect of earth covering and water body on land surface temperature (LST). *J. Civ. Eng., Sci. Technol.* **11**, 45–56 (2020).
128. Du, L. et al. Comparison of two simulation methods of the temperature vegetation dryness index (TVDI) for drought monitoring in semi-arid regions of China. *Remote Sens.* **9**, 177 (2017).
129. Moran, M., Clarke, T., Inoue, Y. & Vidal, A. Estimating crop water deficit using the relation between surface-air temperature and spectral vegetation index. *Remote Sens. Environ.* **49**, 246–263 (1994).
130. Sandholt, I., Rasmussen, K. & Andersen, J. A simple interpretation of the surface temperature/vegetation index space for assessment of surface moisture status. *Remote Sens. Environ.* **79**, 213–224 (2002).
131. Sun, L., Sun, R., Li, X., Liang, S. & Zhang, R. Monitoring surface soil moisture status based on remotely sensed surface temperature and vegetation index information. *Agric. For. Meteorol.* **166**, 175–187 (2012).
132. Tagesson, T. et al. Disaggregation of SMOS soil moisture over West Africa using the Temperature and Vegetation Dryness Index based on SEVIRI land surface parameters. *Remote Sens. Environ.* **206**, 424–441 (2018).
133. Morais, L. F. et al. Spatial and Temporal analysis (2008-2017) of droughts and their effects on livestock in the Brazilian semi-arid region. *An. Acad. Bras. Ciências* **95**, e20220890 (2023).
134. Sandeep, P., Reddy, G. O., Jegankumar, R. & Kumar, K. A. Monitoring of agricultural drought in semi-arid ecosystem of Peninsular India through indices derived from time-series CHIRPS and MODIS datasets. *Ecol. Indic.* **121**, 107033 (2021).
135. Friedman, J. H. Greedy function approximation: a gradient boosting machine. *Ann. Stat.* 1189–1232 (2001).
136. Cortes, C. Support-Vector Networks. *Machine Learning* (1995).
137. Breiman, L. Random forests. *Mach. Learn.* **45**, 5–32 (2001).
138. Prokhorenkova, L., Gusev, G., Vorobev, A., Dorogush, A. V. & Gulin, A. CatBoost: unbiased boosting with categorical features. *Adv. Neural Inf. Process. Syst.* **31** (2018).
139. Hochreiter, S. Long Short-term Memory. *Neural Computation MIT-Press* (1997).
140. Liu, Y., Wang, Y. & Zhang, J. in Proc. Information Computing and Applications: Third International Conference, ICICA 2012, Chengde, China, September 14–16, 2012. 246–252 (Springer, 2012).
141. Li, P. Robust logitboost and adaptive base class (abc) logitboost. *arXiv preprint arXiv:1203.3491* (2012).
142. Ke, G. et al. Lightgbm: a highly efficient gradient boosting decision tree. *Adv. Neural Inf. Process. Syst.* **30** (2017).
143. Mountrakis, G., Im, J. & Ogole, C. Support vector machines in remote sensing: a review. *ISPRS J. Photogramm. Remote Sens.* **66**, 247–259 (2011).
144. Dorogush, A. V., Ershov, V. & Gulin, A. CatBoost: gradient boosting with categorical features support. *arXiv preprint arXiv:1810.11363* (2018).
145. Zhao, Z., Liu, J. & Cox, J. in Machine Learning and Knowledge Discovery in Databases: European Conference, ECML PKDD 2014, Nancy, France, September 15-19, 2014. Proceedings, Part III 14 385-400 (Springer, 2014).
146. Luo, X., Chang, X. & Ban, X. Regression and classification using extreme learning machine based on L1-norm and L2-norm. *Neurocomputing* **174**, 179–186 (2016).
147. Wolpert, D. H. Stacked generalization. *Neural Netw.* **5**, 241–259 (1992).
148. Jain, A. K., Mao, J. & Mohiuddin, K. M. Artificial neural networks: a tutorial. *Computer* **29**, 31–44 (1996).
149. Mann, H. B. Nonparametric tests against trend. *Econometrica: J. Econom. Soc.* 245–259 (1945).
150. Kendall, M. G. *Rank Correlation Methods* (1948).
151. Khaliq, M. N., Ouarda, T. B., Gachon, P., Sushama, L. & St-Hilaire, A. Identification of hydrological trends in the presence of serial and cross correlations: a review of selected methods and their application to annual flow regimes of Canadian rivers. *J. Hydrol.* **368**, 117–130 (2009).
152. Fiala, T., Ouarda, T. B. & Hladný, J. Evolution of low flows in the Czech Republic. *J. Hydrol.* **393**, 206–218 (2010).

153. Yue, S. & Wang, C. The Mann-Kendall test modified by effective sample size to detect trend in serially correlated hydrological series. *Water Resour. Manag.* **18**, 201–218 (2004).
154. Liashchynskyi, P. Grid search, random search, genetic algorithm: a big comparison for NAS. *arXiv preprint arXiv:1912.06059* (2019).
155. Lange, M. A. in EGU General Assembly Conference Abstracts EGU-4991 (2023).
156. Bou-Zeid, E. & El-Fadel, M. Climate change and water resources in Lebanon and the Middle East. *J. Water Resour. Plan. Manag.* **128**, 343–355 (2002).
157. RASOULI, A. A., Babaeian, I., Ghaemi, H. & ZawarReza, P. Time series analysis of the pressure of the synoptic pattern centers affecting on seasonal precipitation of Iran (2012).
158. Shevah, Y. Impact of persistent droughts on the quality of the middle east water resources. *Separation Science and Technology*. Vol 11, 51–84 (Elsevier, 2019).

Acknowledgements

This study was funded by National Sciences and Engineering Research Council of Canada (NSERC) (funding number: RGPIN-2024-06736). The funder played no role in study design, data collection, analysis and interpretation of data, or the writing of this manuscript.

Author contributions

Y.Kh. conceived and designed the study, developed the methodology, implemented the analyses, and wrote the initial draft of the manuscript. T.B.M.J.O. supervised the project, contributed to methodological refinement and data interpretation, and reviewed and edited the manuscript. Both authors discussed the results and contributed to the final version of the paper.

Competing interests

The authors declare no competing interests.

Ethics approval

Not applicable.

Additional information

Supplementary information The online version contains supplementary material available at https://doi.org/10.1038/s43247-025-02359-1.

Correspondence and requests for materials should be addressed to Younes Khosravi or Taha B. M. J. Ouarda.

Peer review information *Communications Earth & Environment* thanks Foyez Ahmed Prodhan and the other, anonymous, reviewer(s) for their contribution to the peer review of this work. Primary Handling Editor: Aliénor Lavergne [A peer review file is available].